Article

Developmental Cell

Activation of Skeletal Stem and Progenitor Cells for Bone Regeneration Is Driven by PDGFRβ Signaling

Graphical Abstract

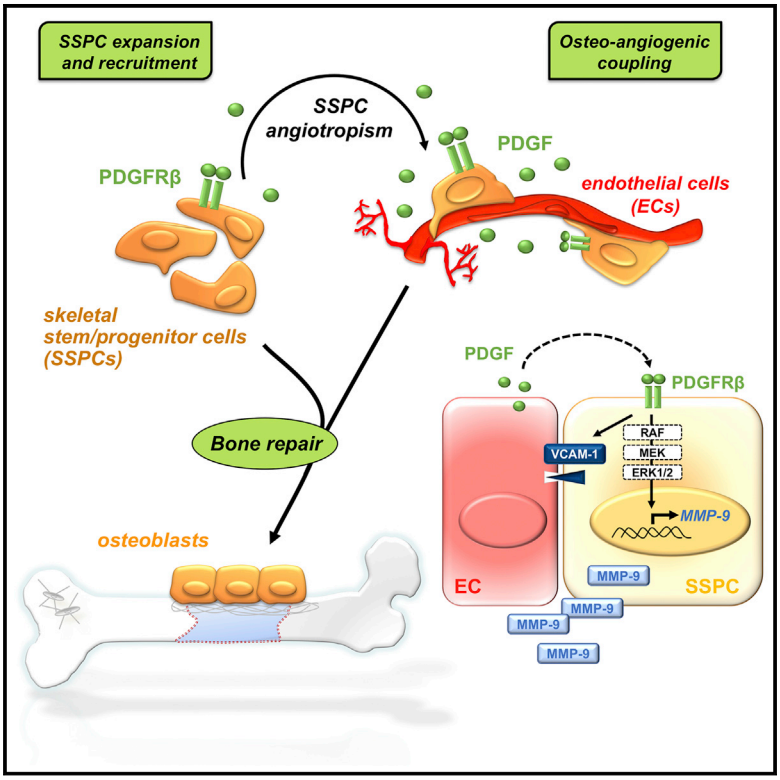

Authors

Anna-Marei Böhm, Naomi Dirckx, Robert J. Tower, ..., Thierry Voet, Matthias Van Hul, Christa Maes

Correspondence

christa.maes@kuleuven.be

In Brief

Böhm et al. show that bone injury activates multiple Osx^{+}-marked cell subsets in the bone and bone marrow environment, representing osteogenesis-competent skeletal stem and progenitor cells (SSPCs). These include PDGFRβ^{+} SSPCs residing in perivascular niches. The authors found that PDGF-PDGFRβ signaling is functionally required to drive the expansion, recruitment, and blood vessel affinity of reparative SSPCs.

Highlights

- Multiple SSPC subsets, broadly marked by Osx^{+} history, are activated by bone injury
- Osteogenesis-competent, stromal, and perivascular SSPCs strongly express PDGFRβ
- Loss of PDGFRβ prevents adequate reparative SSPC expansion and callus formation
- PDGF-PDGFRβ signaling induces SSPC proliferation, trafficking, and angiotropism

Böhm et al., 2019, Developmental Cell *51*, 236–254
October 21, 2019
https://doi.org/10.1016/j.devcel.2019.08.013

CellPress

CellPress

Developmental Cell
Article

Activation of Skeletal Stem and Progenitor Cells for Bone Regeneration Is Driven by PDGFRβ Signaling

Anna-Marei Böhm,[1,6] Naomi Dirckx,[1,6] Robert J. Tower,[1,6] Nicolas Peredo,[1] Sebastiaan Vanuytven,[2] Koen Theunis,[2] Elena Nefyodova,[1] Ruben Cardoen,[1] Volkhard Lindner,[3] Thierry Voet,[2,4] Matthias Van Hul,[1,5] and Christa Maes[1,7,*]

[1]Laboratory of Skeletal Cell Biology and Physiology (SCEBP), Skeletal Biology and Engineering Research Center (SBE), Department of Development and Regeneration, KU Leuven, 3000 Leuven, Belgium
[2]Laboratory of Reproductive Genomics, Department of Human Genetics, KU Leuven, 3000 Leuven, Belgium
[3]Center for Molecular Medicine, Maine Medical Center Research Institute, Scarborough, ME, USA
[4]Wellcome Sanger Institute, Wellcome Genome Campus, Cambridge CB10 1SA, UK
[5]Current address: Metabolism and Nutrition Research Group, Louvain Drug Research Institute, UCLouvain, Université catholique de Louvain, Brussels, Belgium
[6]These authors contributed equally
[7]Lead Contact
*Correspondence: christa.maes@kuleuven.be
https://doi.org/10.1016/j.devcel.2019.08.013

SUMMARY

Bone repair and regeneration critically depend on the activation and recruitment of osteogenesis-competent skeletal stem and progenitor cells (SSPCs). Yet, the origin and triggering cues for SSPC propagation and migration remain largely elusive. Through bulk and single-cell transcriptome profiling of fetal osterix (Osx)-expressing cells, followed by lineage mapping, cell tracing, and conditional mouse mutagenesis, we here identified PDGF-PDGFRβ signaling as critical functional mediator of SSPC expansion, migration, and angiotropism during bone repair. Our data show that cells marked by a history of Osx expression, including those arising in fetal or early postnatal periods, represent or include SSPCs capable of delivering all the necessary differentiated progeny to repair acute skeletal injuries later in life, provided that they express functional PDGFRβ. Mechanistically, MMP-9 and VCAM-1 appear to be involved downstream of PDGF-PDGFRβ. Our results reveal considerable cellular dynamism in the skeletal system and show that activation and recruitment of SSPCs for bone repair require functional PDGFRβ signaling.

INTRODUCTION

Bone formation during development, growth, bone remodeling, and fracture repair fundamentally relies on the activity of mature osteoblasts (OBs). During embryonic osteolineage specification, mesenchymal skeletal stem cells (SSCs) or populations of skeletal stem and progenitor cells (SSPCs) differentiate into committed osteoprogenitor cells (OPCs). The key osteogenic transcription factors, Runx2 and Osterix (Osx), drive OPCs to progress to mature OBs expressing type I collagen (Col1) and later osteocalcin (Zaidi, 2007). The astounding capacity of the skeleton to repair fractures by effectively regenerating bone tissue implies a competence to dynamically generate an adequately sized pool of OBs upon trauma. Major advances have been made recently in the identification and characterization of SSC and SSPC populations, including subsets of bone marrow (BM) stromal cells (BMSCs), in mice (Chan et al., 2015; Marecic et al., 2015; Mendez-Ferrer et al., 2010; Morikawa et al., 2009; Omatsu et al., 2010; Ono et al., 2014b; Worthley et al., 2015; Zhou et al., 2014) and humans (Chan et al., 2018; Sacchetti et al., 2007). Although the relative contributions of distinct SSC and/or SSPC sources to fracture repair remain debated, a number of endogenous, osteogenesis-competent, reparative cell populations have been recognized in the periosteum and within the BM stroma. These SSPC populations were lineage traced or marked by expression of gremlin 1 (Worthley et al., 2015), cathepsin K (Debnath et al., 2018), Osx (Mizoguchi et al., 2014), Prx1 (Duchamp de Lageneste et al., 2018), αSMA (Matthews et al., 2014), Gli1 (Shi et al., 2017), Sox9 (He et al., 2017), or Mx1 (Park et al., 2012). Yet, relatively little is known about the mechanisms and signaling cues that drive resident SSPCs toward repair and regeneration, by steering their local activation, expansion, migration, and differentiation in response to trauma. A better understanding of the cell biology of SSPCs and of the niche-derived signals that convert them from a resting state into regenerative skeletogenic cell lineages could lead to new osteo-anabolic approaches to facilitate repair of non-unions, or even to prevent osteoporosis-induced fractures.

In our preceding lineage tracing of the origin and fate of osteogenic cells in development, we documented that perichondrial Osx^+ OPCs infiltrated fetal bones along with their initial vascular invasion; the cells subsequently expanded, and contributed to the BM stroma and to new bone formation (Maes et al., 2010), indicating that they represent or contain SSPCs. Similar osteo-angiogenic co-invasion was observed during fracture repair (Maes et al., 2010), a process known to largely recapitulate bone development (Dirckx et al., 2013; Gerstenfeld et al., 2003). Intriguingly, a fraction of the recruited Osx^+ OPCs entered

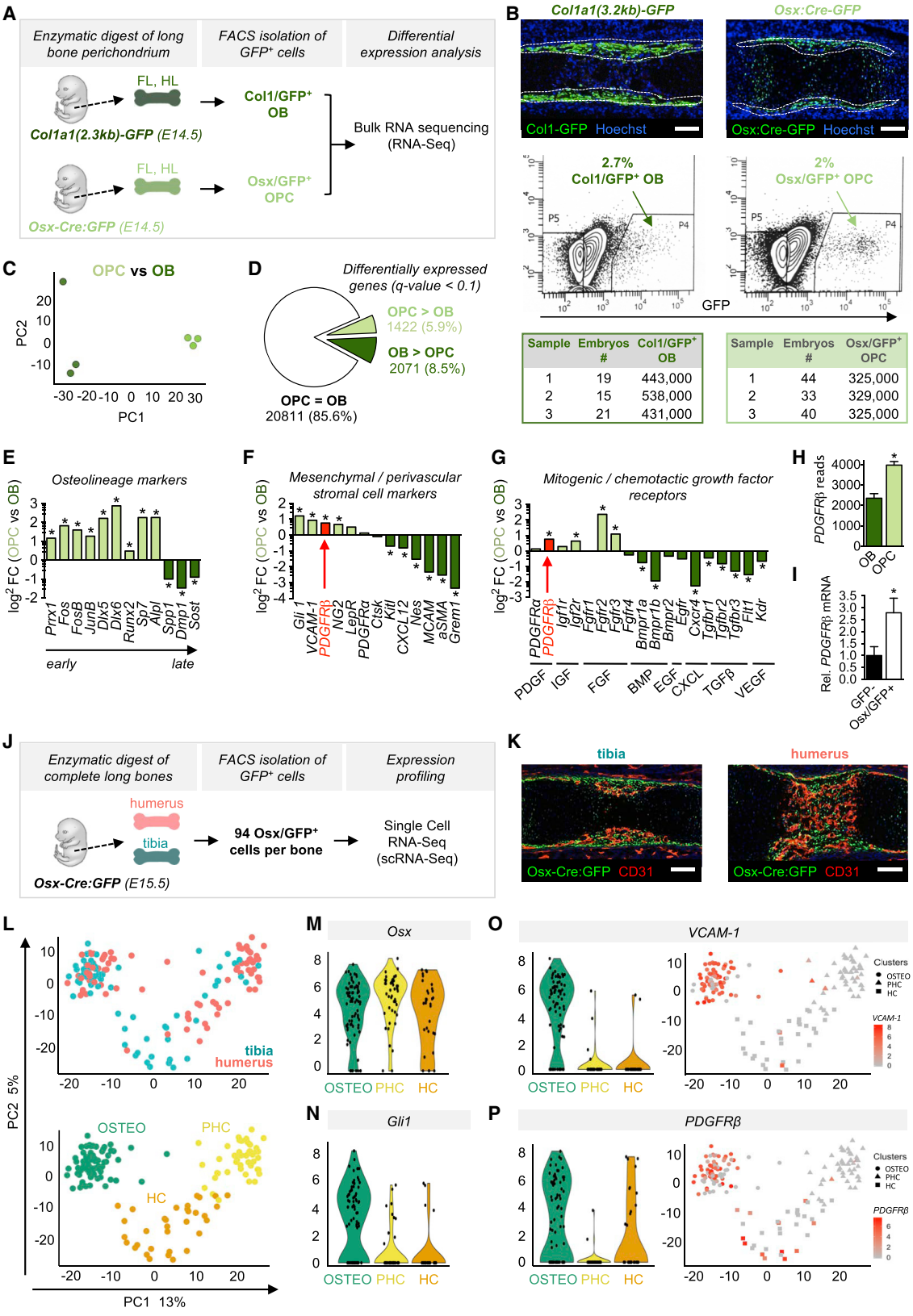

(legend on next page)

developing and healing bones as pericytes, wrapped around the blood vessels (Maes et al., 2010). Perivascular stromal cells in the BM have over the past decade increasingly come into focus, as constituents of hematopoietic niches as well as potential sources of multipotent SSCs or SSPCs (Mendez-Ferrer et al., 2010; Morikawa et al., 2009; Ono et al., 2014a; Sacchetti et al., 2007; Zhou et al., 2014). The existence of a perivascular niche for SSPCs could help explain the absolute necessity of blood vessels for bone (re-)generation and the principle of angiogenic-osteogenic coupling (Kusumbe et al., 2014; Maes et al., 2012; Schipani et al., 2009; Wang et al., 2007).

We here reasoned that uncovering pathways involved in fetal SSPC recruitment and osteo-angiogenic coupling could have therapeutic value for bone repair. Our approach was to analyze Osx$^+$ OPCs, in relation to slightly more differentiated Col1$^+$ OBs. Since the latter did not display strong vascular affinity and migratory behavior during skeletogenesis (Maes et al., 2010), comparative transcriptomics could deliver insights in the molecular underpinnings of these progenitor-specific traits.

Our results identified PDGFRβ, the tyrosine kinase cell-surface receptor for platelet-derived growth factors (PDGFs), as a marker for SSPCs as well as a critical functional driver of SSPC angiotropism and activation during bone repair. Osx$^+$ lineage fate mapping showed that cells with a history of fetal, early postnatal, or constitutive Osx expression distributed throughout the entire adult BM stroma as networks of reticular and perivascular cells, in addition to contributing to periosteal, endosteal, and trabecular bone cells. Upon trauma, these various Osx$^+$ populations became activated to cumulatively generate the SSPC pool producing the repair tissue. Conditional loss of PDGFRβ led to impaired proliferative responses, premature osteogenic differentiation and diminished vascular affinity of SSPCs, altogether cumulating in undersized, improperly composed, and poorly vascularized calluses. Mechanistically, we found that PDGF-PDGFRβ signaling maintains a proliferative, immature, and migratory cell pool with high affinity for blood vessels, which appears to be molecularly mediated at least in part by downstream induction of matrix metalloproteinase (MMP)-9 and by maintaining adequate levels of vascular cell adhesion molecule-1 (VCAM-1). Thus, reparative SSPCs require functional PDGF-PDGFRβ signaling to properly expand, migrate, associate with blood vessels, and mediate callus formation during bone repair.

RESULTS

Extracting the OPC-Specific Gene Expression Signature

In search of mediators of SSPC recruitment and angiotropism, we aimed to extract the specific signature of motile and partly pericytic Osx$^+$ OPCs by differentiating it from the profile of bone-anchored mature OBs. Using Osx(Sp7)-Cre:GFP and Col1a1(2.3kb)-GFP transgenic mice, we isolated Osx/GFP+ OPCs and Col1/GFP+ OBs from their *in vivo* perichondrial environment at embryonic day (E)14.5 for RNA sequencing (RNA-seq) (Figure 1A). To avoid co-isolation of Osx$^+$ prehypertrophic and hypertrophic chondrocytes (PHCs and HCs), we developed a stepwise protocol of partial enzymatic digestion and fluorescence-activated cell sorting (FACS) that allowed us to selectively extract or at least strongly enrich for perichondrial cells (Figure S1A). Three biological samples were collected per subpopulation, each composed of the pooled cell yield from n = 15–44 embryos (Figure 1B). Principle component (PC) analysis confirmed clustering within the groups as well as distance between the cell subsets (Figure 1C). We identified 3,493 (14.4%) differentially expressed genes, of which 1,422 were enriched in OPCs and 2,071 genes were enriched in OBs (Figure 1D). Col1/GFP+ cells strongly expressed markers and pathways related to OB differentiation, cell-cell adhesion, matrix secretion, and cell polarity (Figure S1B), consistent with a phenotype of mature, matrix-secreting OBs. In line with an OPC identity, Osx/GFP+ cells displayed a pro-proliferative profile (Figure S1B) and enriched expression of early but not late osteogenic differentiation markers compared with Col1/GFP+ cells (Figure 1E), validating the stage-specificity of the cell subsets.

Because of our specific interests, we next probed the RNA-seq data for candidate genes related to blood vessel affinity and cellular expansion and recruitment, including (1) markers of perivascular and stromal SSPCs (albeit mostly identified in postnatal bone and BM) (Figure 1F) and (2) receptors of mitogenic and/or chemotactic growth factors (Figure 1G). One of the molecules expressed more strongly in OPCs than in OBs, and in fact fitting both criteria, was PDGFRβ (Figures 1F–1H). Its enriched expression was confirmed in an independent set of sorted Osx/GFP+ cells by qRT-PCR (Figure 1I).

To ensure that the enrichment was pertinent in early osteolineage cells and not caused by contaminating Osx$^+$ chondrocytes,

Figure 1. Extraction of the Fetal Osx$^+$ Osteogenic Progenitor-Specific Molecular Signature

(A) Scheme illustrating the bulk RNA-seq setup. FL, front limb; HL, hind limb. OPC, osteoprogenitor cell; OB, osteoblast. See also Figure S1.

(B) (Top) E14.5 tibia showing Col1/GFP+ and Osx/GFP+ cells in the perichondrium (dashed lines). Scale bars, 100 μm. (Middle) Representative FACS density plots. (Bottom) Numbers of pooled cells per sample (n = 3 biological replicates per cell type).

(C) Principle component analysis (PCA) of OPCs and OBs.

(D) Differentially expressed gene numbers, *padj (q-value) < 0.1 by Benjamini–Hochberg procedure.

(E–G) Differential expression by RNA-seq of (E) osteolineage markers, (F) mesenchymal and perivascular stromal cell markers, and (G) mitogenic and chemotactic growth factor receptors, between Osx/GFP+ OPCs and Col1/GFP+ OBs (n = 3). *padj < 0.1 by Benjamini–Hochberg procedure.

(H) *PDGFRβ* reads in OPCs and OBs, n = 3, *padj < 0.1 by Benjamini–Hochberg procedure.

(I) *PDGFRβ* qRT-PCR in Osx/GFP$^+$ versus GFP$^-$ cells from newborn Osx-Cre:GFP(Tg) mouse long bones, n = 4, *p < 0.05, Student's t test.

(J) Scheme illustrating the scRNA-seq setup.

(K) Tibia and humerus of Osx-Cre:GFP mice at E15.5, with CD31 IHC (red). Osx/GFP$^+$ cells (green). Scale bars, 100 μm.

(L) PCA plots of Osx$^+$ cells, indicating sample origin (top) and 3 main clusters, identified as osteoblasts (OSTEO), pre-hypertrophic chondrocytes (PHC), and hypertrophic chondrocytes (HC) (bottom). See also Figure S2.

(M and N) Violin plots with jittered points of (M) *Osx* and (N) *Gli-1* expression in the single cells of the 3 clusters.

(O and P) Violin plots with jittered points and PCA plots pseudo-colored to indicate the expression levels of (O) *VCAM-1* and (P) *PDGFRβ* in the individual cells. All values represent mean ± SEM. See also Figures S1 and S2.

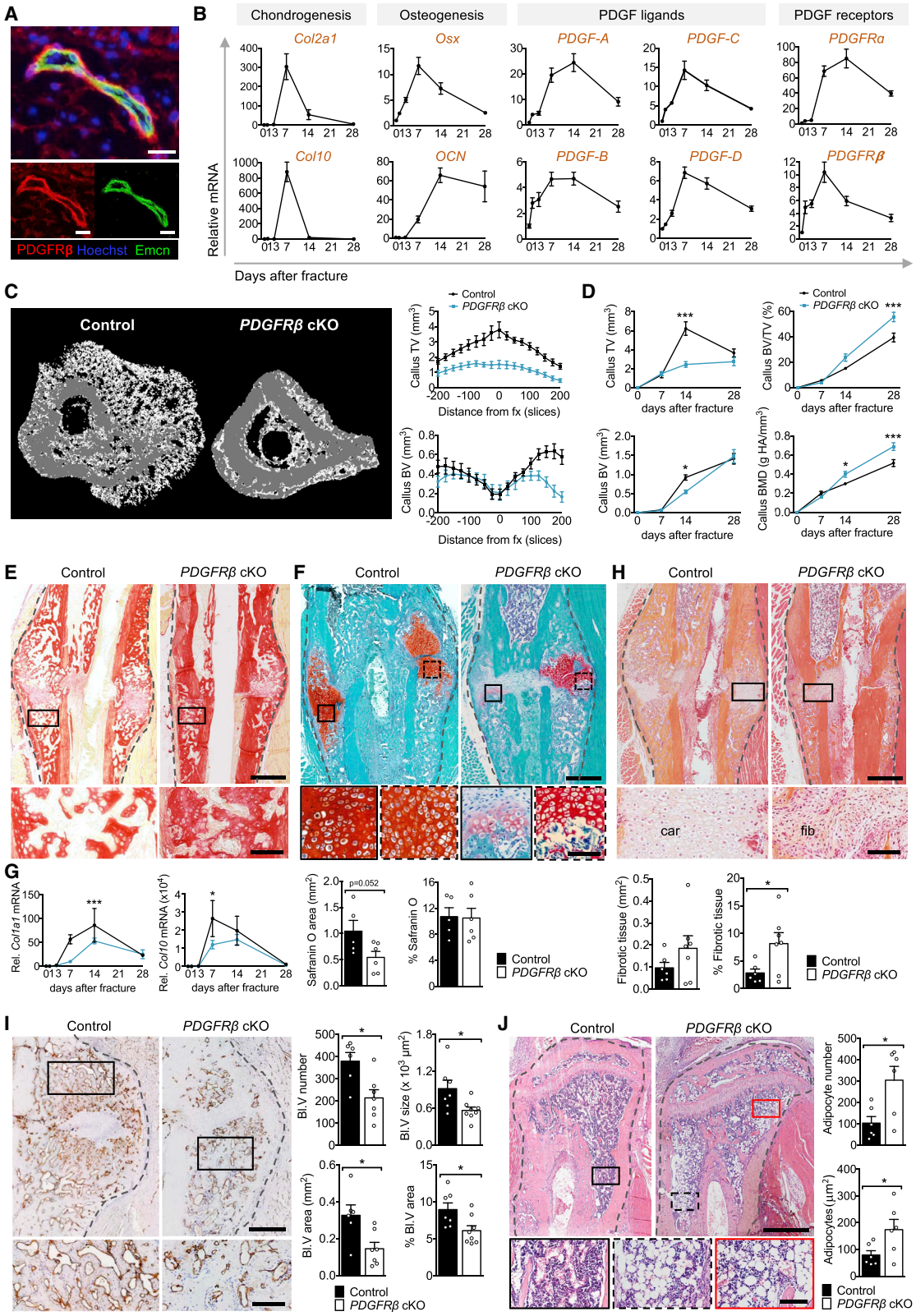

(legend on next page)

and persisted throughout the osteo-angiogenic invasion of developing bones, we performed single cell (sc) RNA-seq. We profiled 188 single Osx/GFP+ cells derived from full digests (not perichondrium-selective as above) of E15.5 Osx-Cre:GFP$^+$ tibias (peri-invasion stage) and humeri (primary ossification center initiated) by SMART-Seq2, of which 157 cells passed the quality control filters (Figures 1J and 1K). Unbiased PC analysis yielded 3 main clusters that, based on marker expression (Figure S2A), were identified as bona fide osteolineage cells, PHCs, and HCs (Figure 1L). Osx expression in each cluster was confirmed (Figure 1M). Out of the SSPC and stromal cell markers that were enriched in Osx/GFP+ cells compared with Col1/GFP+ OBs (see Figure 1F), Gli1, VCAM-1, and PDGFRβ were rather specific for the osteolineage cluster (Figures 1N–1P), whereas neuron-glial antigen 2 (NG2) was most abundant in chondrocytes (Figure S2B). Leptin receptor, PDGFRα, and nestin also showed considerable chondrocytic expression, while some other adult murine (m)BMSC markers were expressed only at very low levels or in few fetal Osx/GFP+ cells (Figure S2B).

Loss of PDGFRβ in Osx$^+$ Osteoprogenitors Impairs Callus Formation during Bone Repair

We next focused on the functional role of PDGFRβ, whose prime ligand PDGF-BB is a promising therapeutic target for bone repair (DiGiovanni and Petricek, 2010). PDGFRβ was robustly expressed in perivascular cells wrapping around callus-invading blood vessels identified by immunohistochemstry (IHC) for endomucin (Emcn) (Figure 2A) or CD31 (see further). We inactivated PDGFRβ using the *Osx-Cre:GFP* strain, comparing *Osx-Cre:GFP(Tg);PDGFRβ$^{(lox/lox)}$* (PDGFRβ conditional knockout [cKO]) mice with *Osx-Cre:GFP(Tg);PDGFRβ$^{(+/+)}$* control littermates throughout the study. Despite confirmed successful targeting (Figures S3A and S3B), conditional loss of PDGFRβ in Osx$^+$ OPCs and their osteolineage cell descendants did not lead to notable defects in skeletal development and growth, or in bone mass and remodeling parameters at adult stages under physiological conditions (Figures S3C–S3K; Tables S1 and S2). However, fracture healing was strongly affected, in line with the vigorous activation of mRNA expression of all PDGF family members immediately following bone trauma and during soft (post-fracture day [PFD]7) and hard callus formation (PFD14) (Figure 2B). Most strikingly, control and PDGFRβ cKO mice subjected to a semi-stabilized tibia fracture model showed prominent differences in the size of the repair callus at PFD14, with a 2.5-fold reduced callus volume in PDGFRβ cKO mice ($p < 0.001$) (Figure 2C). This did not represent a delay but rather a fundamental failure in the transient expansion of the repair tissue in mice lacking PDGFRβ in Osx$^+$ cell-derived populations (Figure 2D). Micro-computed tomography (CT), histological, and molecular analysis of the callus composition at PFD14 revealed that, in absolute terms, the PDGFRβ cKO calluses showed reduced amounts of deposited bone matrix (Figures 2D and 2E) and cartilage tissue (Figure 2F), consistent with reduced *Col1a1* and *Col10* mRNA expression (Figure 2G). Expressed relatively as a fraction of the total callus area, however, the small callus in the mutant mice showed an increased mineralized matrix density as well as a greater fraction of fibrous tissue (Figures 2D and 2H). Interestingly, PDGFRβ cKO mice showed both fewer and smaller callus blood vessels than control animals, cumulating in a prevailing deficit in callus vascularization (Figure 2I). Excessive marrow adipocytes were observed in the fractured bone of the mutants, even in regions distant from the callus such as the metaphysis and epiphysis (Figure 2J), whereas virtually no BM fat was prevalent in the proximal tibia of non-injured bones of either genotype at this age (Figure S3J).

These findings indicated a broad functional involvement of PDGF-PDGFRβ signaling in bone repair and suggested that PDGFRβ in Osx$^+$ cells is essential for the generation of skeletal repair tissue.

Lineage-Mapping Experiments Identify Cells with Osx$^+$ History as SSPCs

To monitor the sources and fates of cells with a history of Osx expression in response to bone trauma, we mapped the Osx-Cre:GFP-marked lineage by thick section confocal microscopy using the mTmG reporter, which reveals a great level of detail because of the membrane-localized GFP in recombined (mG+) cells.

In uninjured postnatal long bones, Osx/mG+ lineage traced cells were abundant in the metaphysis and chondro-osseous junction, in the periosteum and endosteum, lining the trabecular surfaces, and embedded within the bone matrix, conform their inclusion of OBs, bone lining cells and osteocytes (Figure 3A). In addition, although Osx is typically not actively expressed in adult SSPCs or BMSCs at appreciable levels, notably large Osx/mG+ lineage traced populations were observed throughout the BM, where they presented both as networks of reticular stromal cells and as perivascular cells (Figure 3A), indicating that these cells are descendants from cells that had expressed Osx earlier. A few Osx/mG+ adipocytes were also seen in the metaphysis (not shown), yet overall BM adipocytes were very sparse as usual in normal young adult mice. These findings are in line with previous Osx$^+$ fate mapping studies (Liu et al., 2013; Mizoguchi et al., 2014).

Figure 2. Loss of PDGFRβ in Osx$^+$ OPCs Impairs Callus Formation during Bone Repair

(A) IHC of PDGFRβ (red) and Emcn (green) in a PFD7 callus. Blue, nuclei (hoechst). Scale bars, 10 μm.
(B) qRT-PCR in semi-stabilized tibia calluses at different stages, n = 5–6 per time point.
(C) Micro-CT images and quantification of callus bone volume (BV) and tissue volume (TV) of control and PDGFRβ cKO mice at PFD14, n = 5–6.
(D) Callus BV, TV, BV/TV, and bone mineral density (BMD) at different days post-fracture; n = 6–8 per group.
(E) Sirius red staining at PFD14. Scale bars, 1 mm (top) and 200 μm (bottom).
(F) Safranin O staining and quantification at PFD14, n = 5–7. Scale bars, 1 mm (top) and 200 μm (bottom).
(G) *Col1a1* and *Col10* qRT-PCR in control and PDGFRβ cKO calluses, n = 4–8 per time point.
(H) H&E with orange G staining at PFD14 and quantification of fibrous tissue (fib). Car, cartilage. n = 6–7. Scale bars, 1 mm (top) and 200 μm (bottom).
(I) CD31 staining at PFD14 and quantification of the blood vessel (Bl.V) number, size, and area, n = 6–8. Scale bars, 500 μm (top) and 200 μm (bottom).
(J) H&E staining at PFD14 and quantification of the adipocyte number and density, n = 6. Scale bars, 1 mm (top) and 200 μm (bottom).
All values represent mean ± SEM. *$p < 0.05$, ***$p < 0.001$, by two-way ANOVA in (D) and (G) and by Student's t test in (F) and (H)–(J). See also Figure S3.

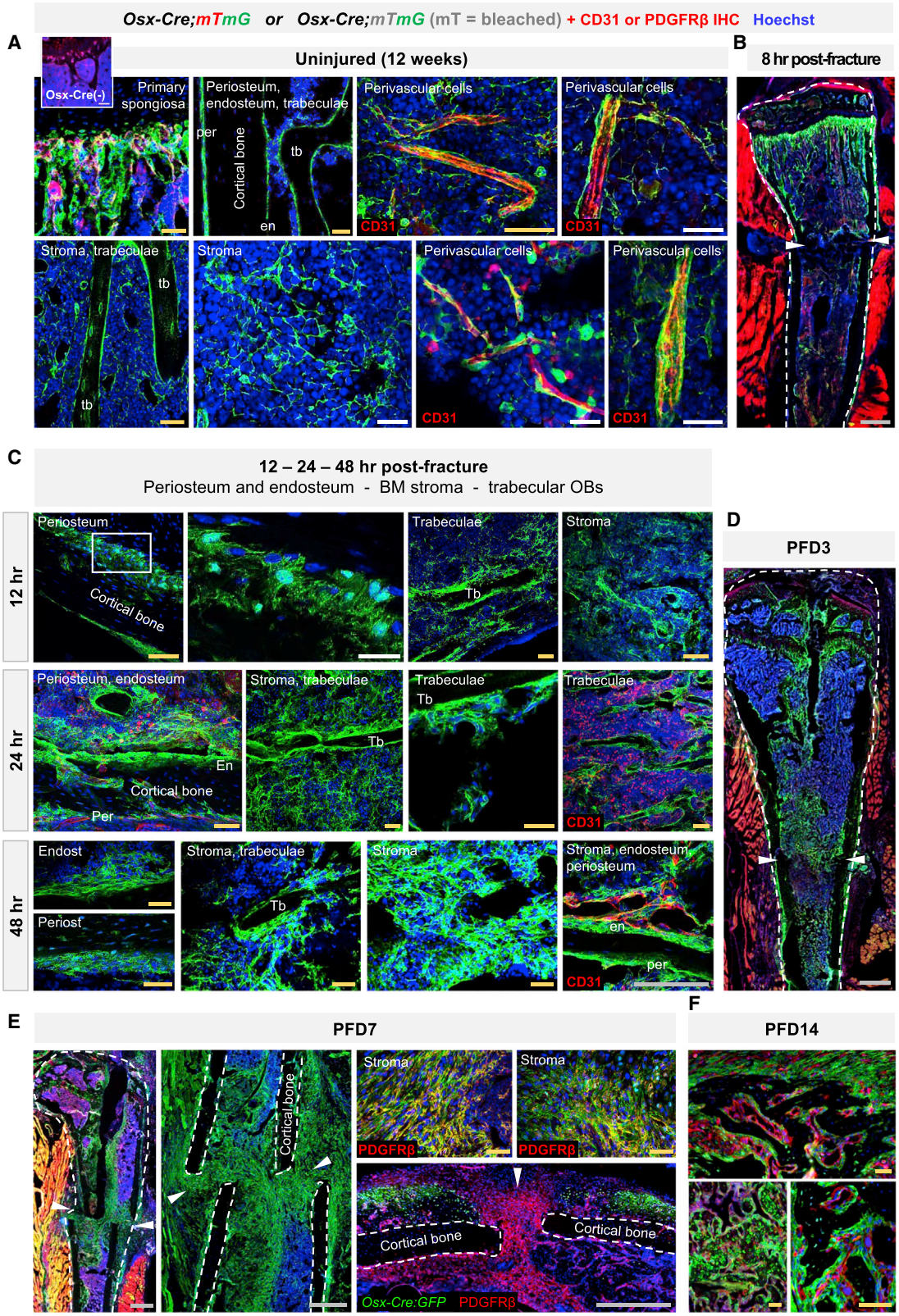

(legend on next page)

Next, we analyzed the dynamic changes in these various Osx/mG+ subpopulations in the semi-stabilized tibia repair model. At 4 and 8 h following fracture induction, no marked alterations were observed in the Osx/mG+ populations (Figure 3B), but from 12 h onwards, manifest responses to the trauma became evident (Figure 3C): the Osx^{+} marked cell subsets, including those localizing to the periosteum, endosteum, BM stroma, and trabecular bone fragments, especially those near the fracture site and the insertion track of the intramedullary fixator, became massively activated as judged by their increased number, altered cell shape, and different spatial orientation. Besides increasingly expanding (12–24–48 h post-fracture), the Osx/mG+ cells attained a directionality perpendicular to the bone surfaces and favoring parallel stromal cell arrangements toward the injury site, suggesting that they were migrating away from their original location, often in close association with blood vessels (Figures 3C, S4A, and S4B). These changes were driven locally by the injury to the bone and BM, as no obvious expansion and spatial remodeling of Osx/mG+ stromal networks or osteolineage populations was observed in contralateral tibia of fractured mice (which looked similar as uninjured tibias of non-fractured mice), excluding major systemic effects.

Extensive mobilization of SSPCs for repair was evident by PFD3, with abundant Osx/mG+ cells presenting throughout the injured bone and BM (Figure 3D). Within the bone defect site and along the intramedullary nail the tibia became increasingly populated with Osx/mG+ cells, appearing mostly as spindle-shaped, directional, fibroblast-like stromal cells at PFD7 (Figure 3E). These cells vigorously expressed PDGFRβ (by IHC), whereas active expression of Osx (detected by the nuclear GFP signal from the Osx-Cre:GFP transgene) indicative of osteolineage commitment, was at this stage restricted to the expanded periosteal areas (Figure 3E). These observations suggest that the bulk of the Osx/mG+;PDGFRβ^{+} cells in the inner callus were undifferentiated SSPCs, which subsequently differentiated into chondrocytes and OBs generating cartilage and bone in the callus as seen by PFD14 (Figures 3F and S4C).

Interestingly, while the Osx/mG+ cells described above represented a continual, lifelong labeling of Osx^{+} cells and their descendants, we observed similar reparative SSPC behavior in cells marked based on their expression of Osx specifically and exclusively in the early postnatal or fetal period. In this experiment, we pulsed inducible Osx-CreERt mice crossed to the tdTomato (tdTom) reporter strain with tamoxifen at postnatal day (P)5 and challenged the mice with a fracture at 3 months of age. At baseline (prior to fracture induction), lineage traced Osx^{P5}/Tom+ cells contributed to the periosteum, endosteum, and cortical and trabecular bone, or were found distributed throughout the adult BM stroma as reticular and perivascular cells, in many cases expressing PDGFRβ (Figure S5A). Upon fracture, the Osx^{P5}/Tom+ population markedly expanded and contributed to the repair: at PFD3 and PFD7, traced cells presented as spindle-shaped cells, expressing PDGFRβ, vigorously proliferating, and associating with blood vessels in the callus area (Figure S5B).

Lineage tracing using Osx-CreERt mice pulsed at E14.5 further revealed that even the earliest fetal population of Osx^{+} cells has the capacity to participate in bone repair in adult life (Figure S5C). Again, fractions of traced Osx$^{E14.5}$/Tom+ cells closely co-localized with skeletal endothelium (Figure S5C).

Thus, mapping the response to bone and BM injury of cells marked by a history of Osx expression revealed their activation as reparative SSPCs and contribution to the various cell types composing the skeletal tissue regenerate.

PDGFRβ Marks SSPCs and their Reparative Progeny in Healing Bones

The small callus in PDGFRβ cKO mice suggested that the expansion and/or mobilization of SSPCs for repair require PDGFRβ signaling. In line with this hypothesis, lineage mapping of PDGFRβ-Cre;mTmG mice revealed that virtually all cells contributing to the repair callus derive from PDGFRβ-expressing cells (Figure 4). In uninjured growing and adult bones, cells marked by PDGFRβ^{+} history (PDGFRβ/mG+ cells) represent the skeletal mesenchyme-derived lineages including growth plate chondrocytes, metaphyseal, periosteal, and endosteal osteolineage cells, cells in the BM stroma and cells in the perivascular space wrapping around Emcn+ blood vessels and CD31+ arteries (Figure S6). Following fracture, by PFD3 a marked activation of PDGFRβ/mG+ cells was observed within the periosteum, endosteum, BM stroma, trabecular bone surfaces, and BM, at all the sites of tissue damage within the environment of the bone defect and the intramedullary nail track, resembling the Osx^{+} cell tracing (see Figure 3), as well as within the injured muscle near the fracture site (Figure 4A). Further lineage tracing indicated that PDGFRβ/mG+ SSPCs cumulatively generated the repair tissue and differentiated into fibroblasts, chondrocytes, and OBs (Figures 4B and 4C).

These data show that PDGFRβ marks reparative SSPCs in the periosteal, endosteal, and perivascular niches, altogether giving rise to osteoblastic, chondrogenic, and fibroblastic progeny in the callus.

PDGF-PDGFRβ Signaling Drives the Expansion of SSPCs for Skeletal Tissue Regeneration

To understand how PDGFRβ signaling in SSPCs functionally acts to mediate bone repair, we investigated the mechanisms

Figure 3. Lineage-Mapping and Cell Fate-Tracing Experiments Identify Cells with a History of Osx Expression as SSPCs

(A) Uninjured Osx-Cre:GFP;mTmG tibia at 12 weeks of age, showing Osx/mG+ cells by GFP IHC. Nuclei are blue by hoechst staining; selected samples include CD31 IHC in red. Inset in upper left panel shows an Osx-Cre(-);mTmG(Tg) control section, lacking GFP signal. Images represent confocal microscopy views, either single optical slices or 5 μm tissue depth projections, except for the primary spongiosa image that represents a projection of 40 μm along the z axis.

(B) Wide-field microscopy overview of an Osx-Cre:GFP;mTmG fractured tibia at 8 h post-fracture.

(C) Calluses at 12, 24, and 48 h post-fracture, showing Osx/mG+ cells by GFP IHC combined with CD31 IHC when indicated. Confocal images represent single optical slices or projections of 5–40 μm along the z axis (tissue depth).

(D–F) Osx-Cre:GFP;mTmG calluses at (D) PFD3, (E) PFD7, and (F) PFD14. Osx/mG+ cells are visualized by GFP IHC, combined with IHC for PDGFRβ when indicated in E (these latter images represent single confocal slice views to accommodate co-localization of the Osx/mG+ and PDGFRβ+ signals).

Arrowheads, fracture site. Per, periosteum; en, endosteum; tb, trabeculae. Scale bars, 500 μm (gray), 50 μm (yellow), 20 μm (white). See also Figure S4 (constitutive Osx+ cell mapping with the mTmG reporter) and Figure S5 (lineage tracing of Osx-CreERt+ cells pulsed with tamoxifen at P5 or E14.5 using tdTom reporter mice).

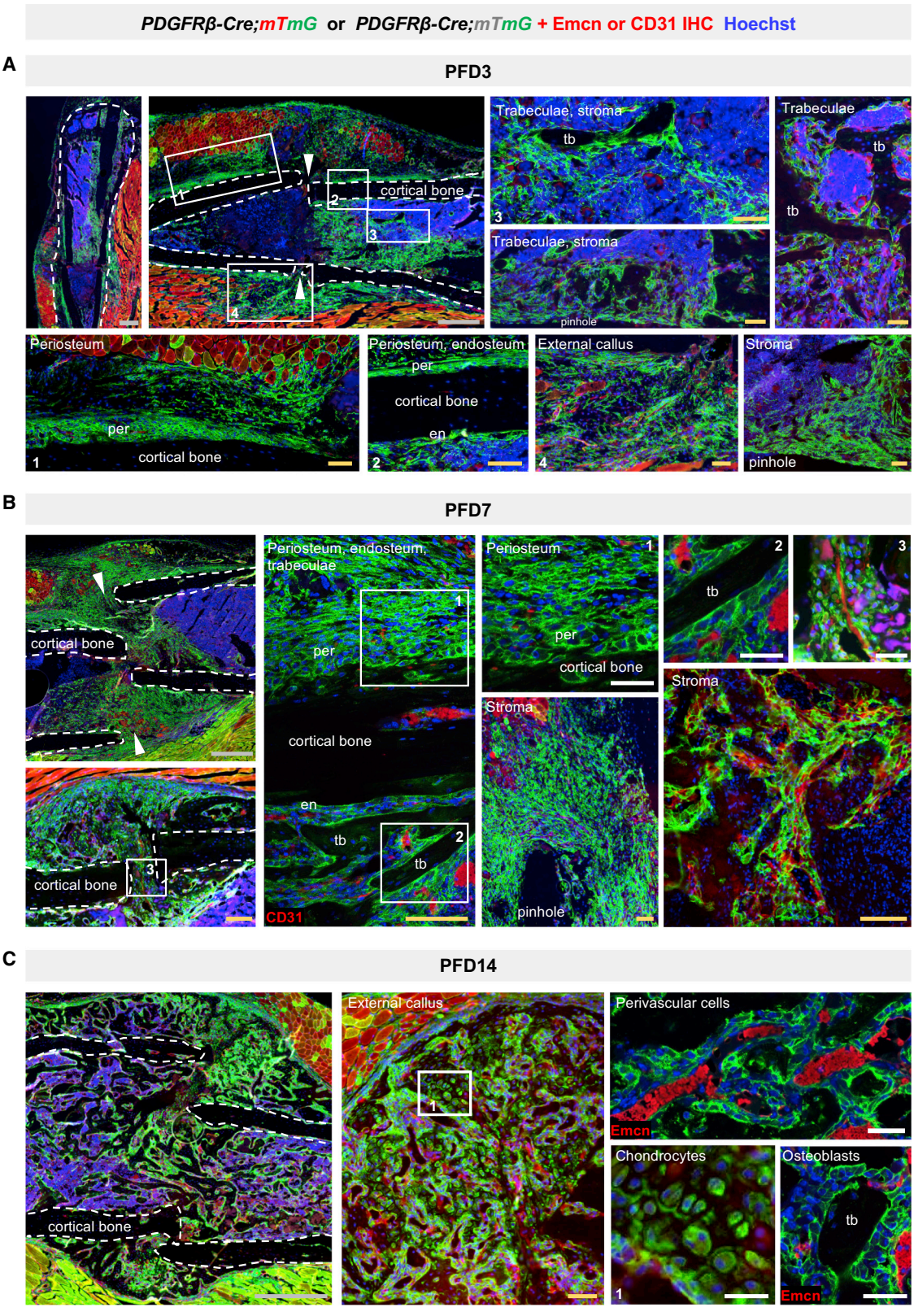

(legend on next page)

underlying the PDGFRβ cKO callus phenotype. We first assessed the implications of PDGF-PDGFRβ signaling in the expansion of the SSPC pool. *In vitro*, rhPDGF-BB was found to be mitogenic for key reparative populations as primary mBMSCs and periosteum-derived cells (mPDCs) (Figures 5A and 5B), while administration of the PDGFRβ inhibitor Imatinib or genetic loss of PDGFRβ (in primary OBs derived from newborn mouse calvaria [mCV OBs]) powerfully blocked cellular expansion (Figures 5A–5C). *In vitro* osteoblastic differentiation and matrix mineralization were inhibited by rhPDGF-BB (Figure 5D) and stimulated by Imatinib (Figure 5E) or by loss of PDGFRβ expression (Figures 5F and 5G). Similar stimulatory effects on proliferation and inhibition of OB differentiation by PDGF-B were seen in a mesenchymal progenitor cell line with osteogenic potential (ST2 cells) (Figure S7). These data suggest that PDGF-PDGFRβ signaling keeps SSPCs in a proliferative, undifferentiated state.

In vivo, the early periosteal cell expansion upon bone trauma was significantly impeded in PDGFRβ cKO mice compared with control littermates (Figure 5H). Moreover, the overall proliferative response throughout the callus was impaired in PDGFRβ cKO mice at PFD3. Especially the number of EdU^+ cells in the BM stroma and endosteum was drastically reduced in the mutant mice, while the activation of cell proliferation in the muscles and tendons adjacent to the defect seemed unaffected (consistent with the lack of Osx/mG+ cells in these regions, see Figure 3) (Figure 5I). Also, qRT-PCR of calluses harvested over a 28-day healing course indicated that loss of PDGFRβ was associated with reduced expression levels of mesenchymal and early osteolineage markers as PDGFRα and Osx (Figure 5J), while markers of mature OBs (Ocn, Dmp1) expressed within normal ranges (Figure 5J), suggesting disproportional osteogenic differentiation.

These results indicate that PDGFRβ signaling is required for SSPCs to proliferate and maintain an immature phenotype during expansion, thereby controlling the generation of a sizable reparative cell pool.

PDGF-PDGFRβ Signaling Induces MMP-9 Expression and Stimulates OPC Migration

We next assessed the involvement of PDGFRβ in the migratory mechanisms of reparative SSPCs. The chemotactic effect of PDGF-BB on OPCs was confirmed using scratch assays with live imaging and endpoint quantification of the wound closure, in MC3T3-E1 osteolineage cells as well as primary mCV OBs (Figures 6A–6D). Moreover, migration of primary cells through a layer of Matrigel matrix in transwell invasion assays was increased by addition of rhPDGF-BB (see further, Figure 6R) and reduced upon genetic inactivation of PDGFRβ (through adenoviral Cre-expression in cultured mCV OBs derived from *PDGFRβ*$^{(lox/lox)}$ mice) (Figure 6E). In search of downstream mediators regulated by the PDGF pathway we mined the fetal Osx/GFP+ scRNA-seq data, focusing specifically on the osteolineage cell cluster. Pathway analysis indicated enrichment of not only extracellular matrix (ECM) and collagen *formation*, but also *degradation* (Figure S8A). Since cell recruitment and migration, as well as angiogenesis (see next section) are highly dependent on tissue remodeling, we surveyed the database for matrix-degrading MMPs. Fetal Osx/GFP+ osteolineage cells expressed several MMPs, to the same magnitude as several housekeeping genes and typical osteolineage products (Figures 6F, 6G, and S8B). Interestingly, higher PDGFRβ levels correlated with higher expression of selected MMPs, including MMP-9 (Figure S8B), an MMP known to be important for fracture healing (Colnot et al., 2003) but historically related to osteoclast rather than OB lineage cells (Vu et al., 1998).

The expression of MMP-9 by osteolineage cells was confirmed. qRT-PCR underscored enrichment in Osx-Cre:GFP-expressing cells within a calvaria lysate (Figure 6H), and the bulk RNA-seq data indicated a high number of reads for MMP-9, especially in OPCs (Figure 6I). *MMP-9* mRNA expression was also detected in a variety of isolated primary murine osteolineage cell subsets (Figure 6J) and osteogenic cell lines (not shown), typically showing levels in the same range as primary bone-derived endothelial cells (ECs) (Figure 6J). IHC localized MMP-9 primarily to actively extending osteo-angiogenic fronts, with part of the signal presenting in and/or around Osx-marked cells, as seen in the fetal perichondrium, postnatal periosteum, metaphysis, and chondro-osseous junction, and in fracture calluses (Figure 6K). Interestingly, functionally blocking MMP-9 activity *in vitro* inhibited the invasiveness of MC3T3 cells (Figure 6L).

We then tested whether PDGF-PDGFRβ signaling may directly regulate MMP-9 expression. Administration of rPDGF-BB to MC3T3 cells consistently upregulated *MMP-9* mRNA, which was inhibited by coinciding treatment with Imatinib (Figure 6M). Selectively MMP-9 was upregulated, while other osteolineage-expressed MMPs were unaffected (Figure 6N). The effect was specific for rPDGF-BB and not elicited by the related growth factors PDGF-DD and vascular endothelial growth factor (VEGF) (Figure 6O). The PDGF-induced MMP-9 transcription appeared to involve MAPK/ERK (Ras-Raf-MEK-ERK) signaling downstream of PDGFRβ, but not the PI3K/Akt pathway, in MC3T3 and ST2 cells (Figures 6P, S8C, and S8D). In line with these results, primary calvarial osteolineage cells from PDGFRβ cKO mice showed reduced expression of MMP-9, but not of other MMPs, compared with cells derived from control littermates (Figure 6Q). Finally, functional validation in primary mBMSCs indicated that their invasiveness through matrix was enhanced by rPDGF-BB, while this stimulation was neutralized by inhibiting MMP-9 activity (Figure 6R).

These data indicate that PDGFRβ activation in osteolineage cells induces a pro-migratory, pro-invasive response, which seems at least *in vitro* to be partly mediated by MMP-9 as direct downstream effector of a PDGF-PDGFRβ-MEK-ERK signaling cascade.

Angio-Osteogenic Crosstalk via PDGF/PDGFRβ and VCAM-1 Regulates Angiotropism of SSPCs

Given the perivascular location of many PDGFRβ-expressing and PDGFRβ/mG+ traced cells, and the vascular deficit in

Figure 4. PDGFRβ Marks SSPCs and their Reparative Progeny in Healing Bones

(A–C) PDGFRβ-Cre;mTmG calluses at PFD3 (A), PFD7 (B), and PFD14 (C). Red, mTomato/CD31/Emcn, as indicated; blue, nuclei (hoechst); big arrowheads, fracture site. Scale bars, 500 μm (gray), 100 μm (yellow), and 50 μm (white). Note abundant expanded and activated PDGFRβ/mG+ cells in the metaphysis, endosteum (en), periosteum (per), along trabeculae (tb), in the callus stroma and around the pinhole. See also baseline PDGFRβ/mG+ analysis in Figure S6.

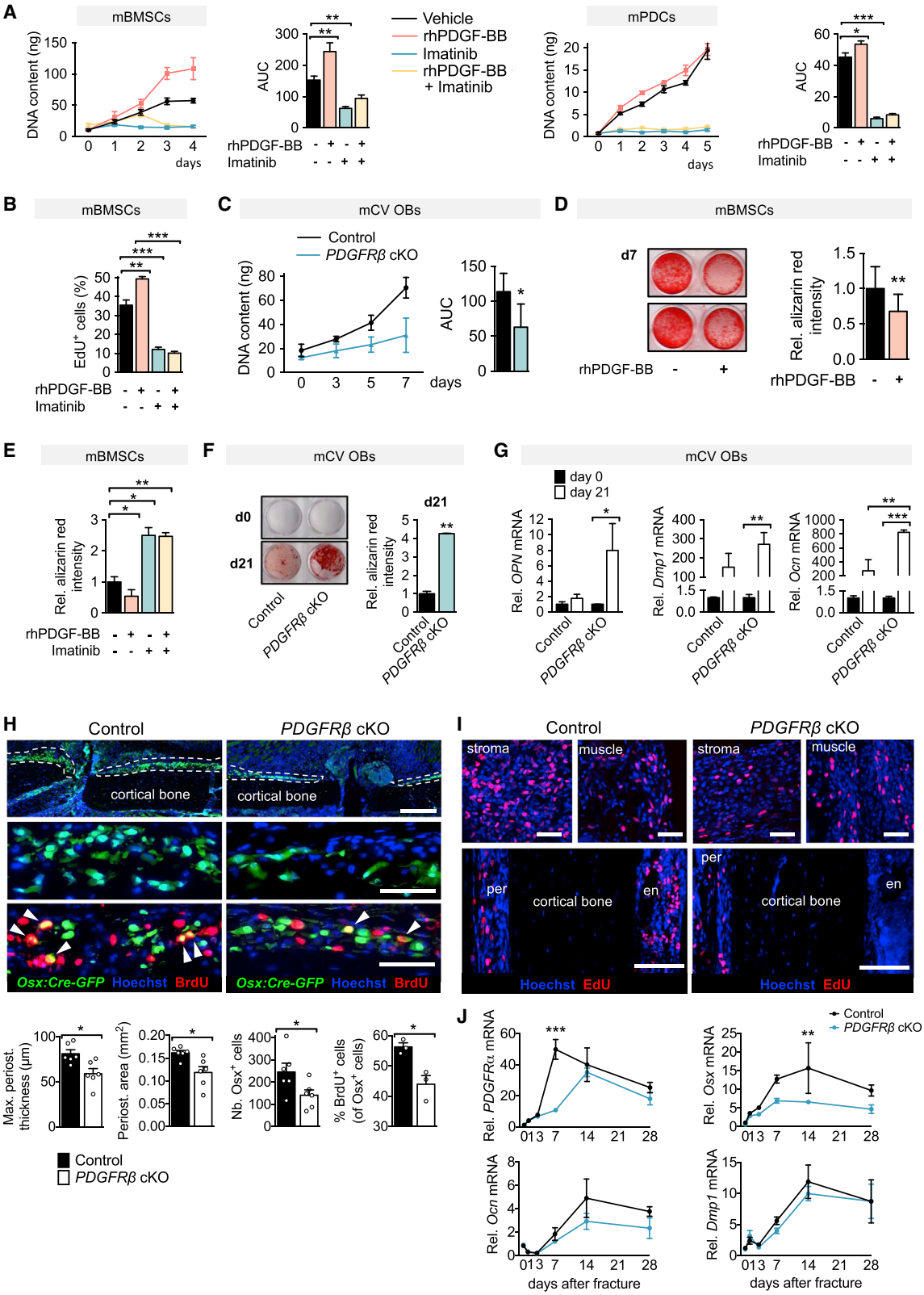

(legend on next page)

PDGFRβ cKO calluses, we specifically addressed the role of PDGF-PDGFRβ signaling in the crosstalk between ECs and PDGFRβ+ SSPCs and OPCs. Using fetal, adult, and fracture callus-derived primary EC populations, we found the PDGFRβ ligands PDGF-B and PDGF-D to be produced by skeletal ECs (and by primary osteoclasts in the case of PDGF-B, in line with Xie et al., 2014) (Figure 7A). Next, we tested the hypothesis that EC-derived PDGF may elicit angiotropic migration of PDGFRβ$^+$ OPCs. Co-cultured ECs as well as EC-conditioned medium exerted strong chemotactic effects on MC3T3 cells (Figure 7B) and mCV OBs (not shown), which was partially or fully blunted by addition of PDGFRβ inhibitors (Figure 7C). To functionally test whether PDGFRβ could control recruitment of OPCs to perivascular locations, we performed tubule assays. Seeding osteogenic cells onto preformed Matrigel-induced EC networks (HUVEC or MS1) led to their quick and nearly complete association with the endothelial tubules (Figure 7D; Videos S1 and S2). This association was reduced by pharmacologic or genetic inhibition of PDGFRβ (Figure 7D).

Likewise, *in vivo*, the association of Osx-Cre:GFP$^+$ cells with callus blood vessels was impeded in PDGFRβ cKO mice relative to controls (Figure 7E). Nearest neighbor distance analyses confirmed that on average, the distance between an Osx/GFP+ cell and the nearest blood vessel was increased in PDGFRβ cKO mice, with a particular reduction in the fraction of Osx/GFP+ cells residing within 2 μm from a vessel (Figure 7F). Of note, besides loss of PDGFRβ, the expression of PDGF-B and PDGF-D was also significantly reduced in PDGFRβ cKO calluses (Figure 7G), suggesting a bidirectionally compromised capacity for osteo-angiogenic coupling mechanisms.

Our RNA-seq data had highlighted the adhesion molecule VCAM-1 as enriched in fetal Osx/GFP+ OPCs compared with more mature OBs (Figure 1F) and revealed its highly selective expression in the osteolineage cluster (Figure 1O). Following up on these transcriptome-based observations, we found that mCV OBs with genetic inactivation of PDGFRβ showed reduced VCAM-1 expression (Figure 7H). VCAM-1 was strongly expressed by early osteogenic cells (Figures 7I and 7J), and bone-derived ECs were found to express the very late antigen-4 (VLA-4) receptor to which VCAM-1 binds (consisting of the integrin subunits α4 and β1) (Figure 7K). This suggests the capacity for osteo-angiogenic interactions resembling the intercellular adhesion documented between pericytes and blood vessels during active neovascularization (Garmy-Susini et al., 2005). *In vivo*, a subset of VCAM-1-expressing cells indeed co-localized with Osx/GFP+ cells in fetal bone, and attained perivascular positions in adult bone (Figure 7L). Functionally, over-expression of VCAM-1 in osteogenic cells enhanced their capacity to associate with EC tubules in the Matrigel tubule assay (Figure 7M) and to adhere to ECs in monolayer culture (Figure 7N).

Altogether, these findings implicate PDGF-PDGFRβ signaling and possibly downstream VCAM-1 in the crosstalk between ECs and SSPCs, mediating the affinity of PDGFRβ$^+$ SSPCs for blood vessels.

Impaired Upregulation of MMP-9 and VCAM-1 during Fracture Repair in PDGFRβ cKO Mice

IHC on PFD7 callus tissues from PDGFRβ-Cre;mTmG-expressing mice revealed that during fracture healing, VCAM-1 localization correlated strongly with cells marked by PDGFRβ, which abundantly populated the internal and external callus regions (Figure 8A). In the callus of PDGFRβ cKO mice, as expected the *PDGFRβ* mRNA and protein expression was blunted (Figures 8B and 8C). Concomitantly, the presence of VCAM-1 and MMP-9 was drastically reduced in PDGFRβ cKO calluses compared with controls (Figure 8B). Upregulation of *VCAM-1* mRNA expression in the course of the healing process was markedly delayed in the mutant mice, while *MMP-9* induction largely failed (Figure 8C).

These data support the possibility that MMP-9 and VCAM-1 may contribute to fracture healing by affecting cell migration, tissue remodeling, and angiotropism of SSPCs downstream of PDGFRβ. Further *in vivo* studies evaluating the functional roles of osteolineage MMP-9 and VCAM-1 will thus be of interest.

DISCUSSION

For the skeleton to repair a defect and regain its proper architecture, sufficient functional OBs must be replenished from endogenous stem or progenitor cell populations. The capacity of the skeleton to regenerate bone thus depends on SSPCs to (1) be activated to propagate, (2) reach the site of the defect, and (3) differentiate into OBs at the sites in need of new bone formation. We here showed that Osx$^+$ SSPCs are capable of delivering all the necessary differentiated progeny to repair acute skeletal injuries later in life, provided that they express functional PDGFRβ.

Figure 5. PDGF-PDGFRβ Signaling Drives Expansion of SSPCs for Skeletal Tissue Regeneration

(A) Growth curves and quantification of areas under the curve (AUC) for primary mBMSCs and mPDCs, treated as indicated; n = 3–4; one-way ANOVA and Dunnett's post-hoc test.

(B) EdU incorporation in mBMSCs treated with vehicle, rhPDGF-BB and/or Imatinib; n = 3; one-way ANOVA.

(C) Growth curve of mCV OBs from control and PDGFRβ cKO newborns; n = 3; t test.

(D and E) Alizarin Red (AR) staining and quantification following osteogenic differentiation of mBMSCs for 7 days. (D) Images show two representatives of n = 6 quantified pools; paired t test. (E) n = 3, paired one-way ANOVA.

(F and G) 21-day osteogenic differentiation of mCV OBs from control and PDGFRβ cKO mice, showing (F) AR analysis (t test) and (G) qRT-PCR of *OPN*, *Dmp1* and *OCN* (n = 2–3; two-way ANOVA and Tukey's post-hoc test).

(H) GFP and BrdU IHC showing callus periosteum at PFD3. Osx/GFP+ cells (green), nuclei (blue, hoechst), BrdU (red). Dashed lines, periosteum; arrowheads, BrdU$^+$/Osx/GFP+ nuclei. Scale bars, 500 μm (top) and 50 μm. n = 6 for periosteal thickness, area, and Osx$^+$ cell number, n = 3 for % of BrdU$^+$/Osx$^+$ cells; Student's t test.

(I) EdU staining (red) of stroma, muscle, endosteum (en) and periosteum (per) in control and PDGFRβ cKO calluses at PFD3. Nuclei (blue), hoechst. Scale bars, 50μm (top), 100 μm (bottom).

(J) qRT-PCR of *PDGFRα*, *Osx*, *OCN* and *Dmp1 at different time points post-fracture*, n = 4–8 calluses per time point, two-way ANOVA.

Values, mean ± SEM. *p < 0.05, **p < 0.01, ***p < 0.001. See also Figure S7.

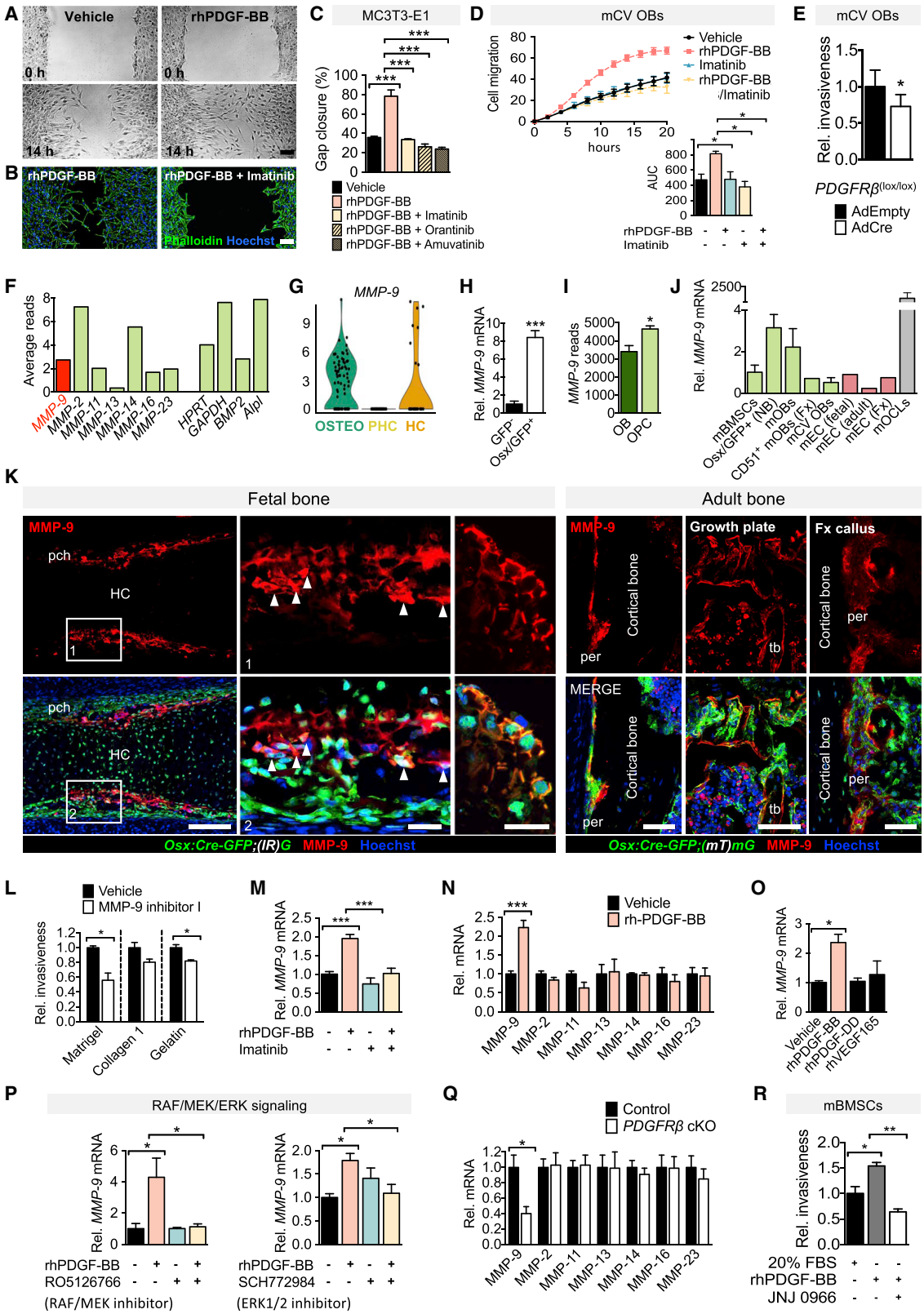

(legend on next page)

Our data revealed that PDGF-PDGFRβ signaling represents a critical mediator of reparative SSPC expansion, migration, and angiotropism. Defects in these three mechanisms contributed to the generation of an undersized, improperly composed, and poorly vascularized callus in mice lacking PDGFRβ in SSPCs.

Identification of the PDGF Pathway as Molecular Determinant of Reparative SSPC Activation

Although several recent studies identified SSC and SSPC populations, our knowledge of the biological signals that activate skeletogenic cells and regulate cell recruitment and the spatial control of bone formation, is still sparse. Previously, FGF-2 has been related to reparative progenitor cell proliferation (van Gastel et al., 2014), the stromal-derived factor (SDF)-1/CXCL12-CXCR4 axis and TGFβ to recruitment and chemotaxis (Dirckx et al., 2013; Tang et al., 2009; Yellowley, 2013), bone morphogenetic proteins (BMPs) to differentiation and osteogenesis (Salazar et al., 2016; Tsuji et al., 2006), and VEGF and its homologue placental growth factor (PlGF) to angiogenesis during fracture healing (Jacobsen et al., 2008; Maes et al., 2006, 2012). As outlined in this work, the PDGF pathway provides a powerful blend of coordinated responses required for bone repair, by combining strong mitogenic, chemotactic, and angiogenic effects. In line with an important functional role in the early and intermediate stages of the repair process, acute skeletal injury stimulated expression of PDGF ligands and receptors in the early fracture hematoma and callus. In addition, some of the immediate responses to trauma include PDGF release from platelets, and hypoxia-induced production of growth factors as PDGFs and VEGFs that can act synergistically and modulate the level of PDGFR signaling (Bouletreau et al., 2002; Schito et al., 2012). PDGF-BB, the main ligand of PDGFRβ, had been amply documented to be mitogenic and chemotactic for osteolineage cells *in vitro* (Fiedler et al., 2004; Ozaki et al., 2007) and to be a vital early initiator of wound healing (Andrae et al., 2008). By demonstrating the role of the PDGF pathway in the molecular control of endogenous SSPC activation for bone regeneration, our study provides *in vivo* evidence of the implications of these activities in fracture repair, bringing new mechanistic clues into how injury-induced changes in the skeletal microenvironment lead to tissue repair.

Loss of PDGFRβ in Osx$^+$ SSPCs impaired the early proliferative responses, but also led to accelerated differentiation. Premature osteogenic differentiation and bone deposition may have further precluded adequate expansion of the reparative SSPC pool, explaining the undersized yet densely mineralized callus of the cKO mice. Our findings, thus, suggest that PDGFRβ is required to maintain the immature, proliferative, and motile nature of SSPCs, possibly particularly those in the perivascular niches.

PDGF-PDGFRβ Signaling Mediates Pericytic Recruitment of SSPCs to Blood Vessels and Osteo-Angiogenic Coupling during Bone Repair

Angiogenesis is vital for bone formation, and in turn, the growth and integrity of the skeletal vascular network is determined by factors produced by bone cells, such as VEGF (Maes et al., 2012; Schipani et al., 2009; Wang et al., 2007). During endochondral bone development and repair, the avascular cartilage intermediate is co-invaded by blood vessels and skeletal progenitors, with a fraction of the recruited mesenchymal cells entering the tissue as pericytes (Maes et al., 2010). The peri-endothelial localization of SSPCs implies direct crosstalk between these osteogenesis-competent cells and the ECs of the growing vasculature, which we here show involves PDGF-PDGFRβ signaling. Indeed, in the fracture callus of PDGFRβ cKO mice, pericytic association of SSPCs with vessels was reduced; concomitantly, angiogenesis and osteogenesis were imbalanced, as callus

Figure 6. PDGF-PDGFRβ Signaling Induces *MMP-9* Expression and Stimulates OPC Migration

(A) Selected images of live imaged scratch assays of rhPDGF-BB-treated MC3T3 cells. Bar, 10 μm.

(B) Scratch assay with MC3T3 cells treated as indicated. Green, phalloidin (actin); blue, hoechst (nuclei). Bar, 10 μm.

(C) Quantification of gap closure of MC3T3 cells treated as indicated; n = 3, one-way ANOVA.

(D) Live cell analysis of migration in a gap closure assay of mCV OBs (n = 4 for vehicle, rhPDGF-BB and Imatinib treatments; n = 2 for rhPDGF-BB+Imatinib). AUC analysis, one-way ANOVA.

(E) Quantification of cellular invasion through Matrigel in transwells using mCV OBs from *PDGFRβ$^{(flox/lox)}$* mice, transduced with adenoviruses expressing Cre (AdCre) or empty vector (AdEmpty); n = 3; *p < 0.05, Student's t test.

(F) Average expression of various MMPs in the scRNA-seq osteolineage cluster cells. For reference, 2 housekeeping genes (*HPRT*, *GAPH*) and 2 typical osteolineage products (*BMP2*, *Alpl*) are shown.

(G) Violin plots with jittered points of *MMP-9* in fetal limb Osx$^+$ cells from the scRNA-seq.

(H) qRT-PCR of *MMP-9* in Osx/GFP+ versus GFP$^-$ cells isolated from long bones of Osx:Cre-GFP mice at E14.5; n = 3-cell pools, each from multiple embryos; ***p < 0.001 by Student's t test.

(I) Expression of *MMP-9* in Osx/GFP+ OPCs and Col1/GFP+ OBs by bulk RNA-seq; n = 3; *p < 0.05.

(J) *MMP-9* qRT-PCR in various subsets of primary osteolineage cells (green bars), skeletal ECs (red bars), and osteoclasts (mOCL) (gray bar). NB, newborn; mOBs, postnatal long bone-derived OBs; Fx, fracture callus-derived. mBMSCs and mOBs, n = 4 independent cell pools; Osx/GFP+ cells, n = 2-cell pools each consisting of cells from multiple mice; CD51$^+$ mOBs (Fx), CD31$^+$ mECs (Fx), pooled sorted cells from 6 calluses; mCV OBs, n = 3; mECs (fetal), pooled cells from multiple embryos; mECs (adult), pooled cells from 4 mice; mOCLs, n = 3. See STAR Methods for details.

(K) IHC of MMP-9 in fetal (E 15.5) bone of Osx-Cre:GFP;IRG mice and in adult (12-week-old) Osx-Cre:GFP;mTmG mice. (Green) Nuclear GFP denotes active Osx expression, cellular GFP marks cells with present or historical Osx expression, (red) MMP-9 IHC, (blue) nuclei stained with hoechst. HC, hypertrophic chondrocytes; Per, periosteum; Tb, trabecular bone; Pch, perichondrium. Arrowheads, Osx-Cre:GFP;IRG+/MMP-9+ cells. Scale bars, 100 μm (fetal left), 20 μm (fetal middle and right) and 50 μm (adult).

(L) Relative invasiveness through Matrigel, collagen 1 and gelatin of MC3T3 cells, pre-treated with vehicle or MMP-9 inhibitor I; n = 3, *p < 0.05 by Student's t test.

(M–O) qRT-PCR of osteolineage-expressed *MMP*s in MC3T3 cells; (M) n = 6–9, (N) n = 3–5, (O) n = 3; one-way ANOVA.

(P) *MMP-9* qRT-PCR in MC3T3 cells treated as indicated; n = 2–12; one-way ANOVA.

(Q) qRT-PCR of *MMP*s in mCV OBs from control and PDGFRβ cKO mice; n = 6; one-way ANOVA.

(R) Invasion through Matrigel of mBMSCs exposed to medium with 20% FBS or 1% FBS + rhPDGF-BB, either or not pre-treated with the pro-MMP-9 activation inhibitor JNJ 0966; n = 3; one-way ANOVA. Values, mean ± SEM. *p < 0.05, **p < 0.01, ***p < 0.001. See also Figure S8.

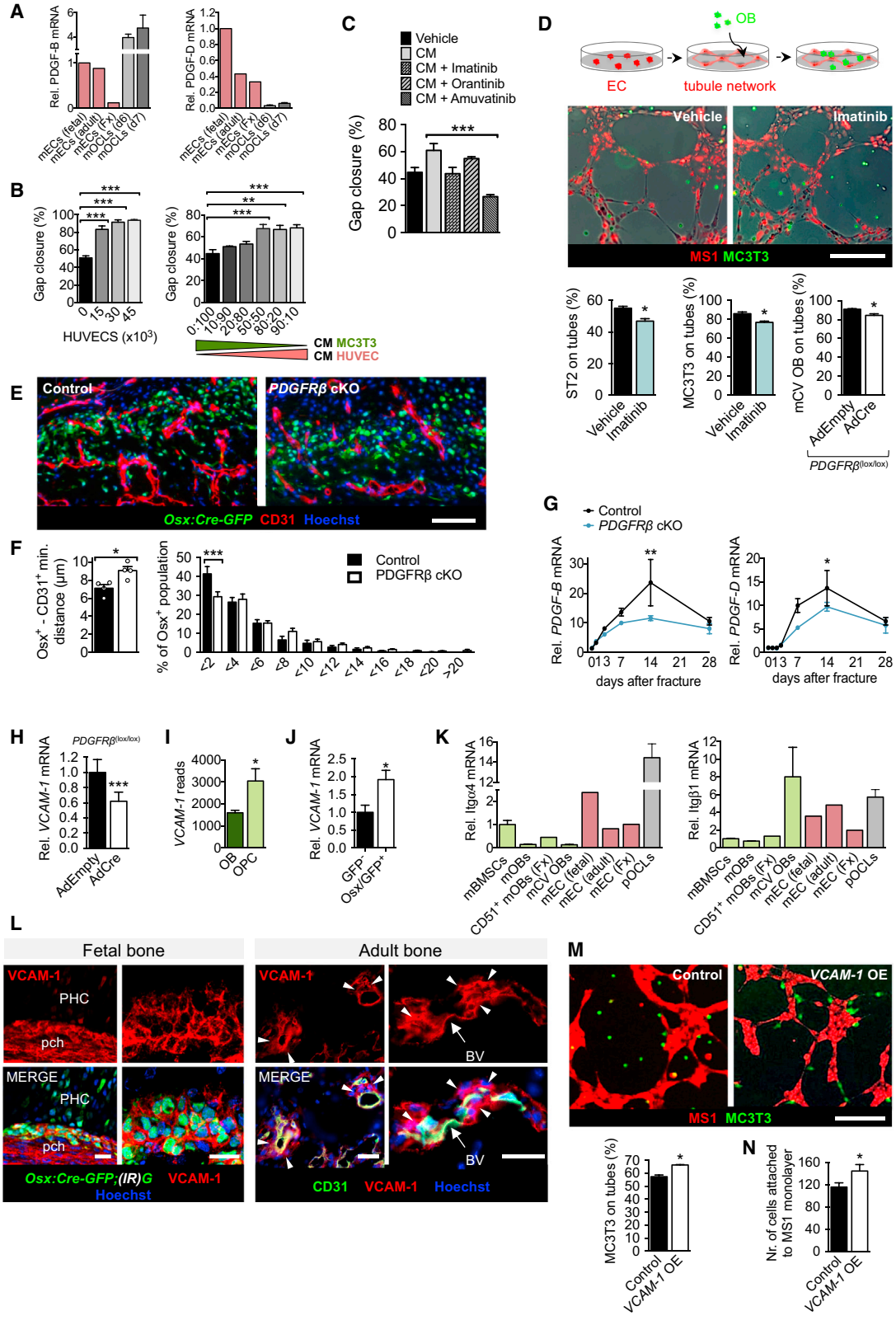

(legend on next page)

vascularization was impaired while ossification occurred prematurely. Albeit not directly proving a causal relationship, these concurrent observations support that these two aspects may be functionally linked and molecularly coupled through PDGFRβ signaling. Blood vessels may provide both niches for pericytic SSPCs to be maintained in an immature state, and guiding cues for their trafficking to bone formation sites. In turn, the SSPCs may stimulate vascular growth and osteo-angiogenic tissue invasion by producing MMP-9, in addition to potentially exerting a stabilizing function on the vessel wall, which may involve VCAM-1 as in vascular development (Garmy-Susini et al., 2005). Our finding that MMP-9 is downstream of PDGF is in line with a study of tracheal smooth muscle cells (Lee et al., 2007), and the importance of MMP-9 in fracture healing was evident in MMP-9 null mice (Colnot et al., 2003; Wang et al., 2013). Although skeletal MMP-9 production has been classically associated primarily with osteoclastic cells (Vu et al., 1998), EC-derived MMP-9 was very recently reported to contribute to cartilage turnover during bone growth (Romeo et al., 2019). Although the *in vivo* role is still uncertain, others' work (McClelland et al., 1998) and ours suggest that osteoblastic MMP-9 may provide significant contributions. Given the primary localization to actively extending osteo-angiogenic fronts, our data raise the possibility that the angiotropism and recruitment of SSPCs to fracture sites are co-directed by a PDGF-PDGFRβ-MMP-9 pro-migratory signaling cascade.

The notion that PDGFRβ may couple callus vascularization and SSPC recruitment harmonizes several of its known functions. Firstly, PDGF-PDGFRβ signaling has been well characterized in vascular biology to recruit mural cell progenitors to the blood vessel wall. Null mice for either PDGF-B or PDGFRβ die due to hemorrhages and edema caused by pericyte deficiency and resultant leaky, non-matured vessels (Hellström et al., 1999; Lindahl et al., 1997). The established model in several organs is that EC-produced PDGF-B attracts PDGFRβ$^+$ mural and stromal cells to the blood vessel (Andrae et al., 2008; Armulik et al., 2011). Our data suggest a parallel mechanism in the skeleton, with PDGF attracting PDGFRβ$^+$ SSPCs to their perivascular niches, although additional signals must be involved as well, given the significant and consistent yet relatively modest defects observed in the osteo-angiogenic interplay. Secondly, PDGF fulfills all the criteria of a common chemo-attractive signal sensed by both SSPCs and ECs, which could steer their coinciding movement and co-invasion. PDGF is also angiogenic and can directly stimulate EC proliferation and migration. Moreover, it has been shown that PDGF-B produced by pre-osteoclasts stimulates angiogenesis and bone remodeling (Xie et al., 2014).

Thus, the working model that reconciles our data and the broader literature is that not only osteoclasts but also skeletal ECs produce PDGF, which provides a directional chemo-attractive signal steering PDGFRβ$^+$ SSPCs toward the blood vessel. As a result of the signaling, the SSPC produces more MMP-9, mediating the tissue remodeling required for the osteo-angiogenic co-invasion of the repair tissue. VCAM-1 could help keep SSPCs and ECs in close juxtaposition, by interacting with its receptor VLA-4 (α4β1 integrin) on the endothelium. Other sources of PDGF likely contribute to the overall effects of PDGFRβ signaling during bone repair, such as PDGF released by platelets in the fracture hematoma, which may be the initial trigger of the early mitogenic and chemotactic responses of the SSPC populations to the trauma.

Master Stem Cell-Centered Hierarchical Model versus Cellular Plasticity among Skeletal Lineages

The sources of reparative SSPCs remain debated, with some studies highlighting the contributions by stem cells within the periosteum and others recognizing prime roles for distinct populations in the BM stroma. The unambiguous identification of SSCs is of high interest in the field; the ambition is to build a lineage ontogeny and differentiation map for the mesenchyme-derived skeletal cell types, in analogy of the well-characterized hematopoietic cell hierarchy. Recent seminal publications have supported the existence of a cell-surface markers-identifiable SSC at the top of the tree, giving rise to multipotent progenitor cells that on their turn can generate progeny forming bone, cartilage, and stroma (Chan et al., 2015, 2018). Complementary to such a master SSC-centered model, however, our findings

Figure 7. Angio-Osteogenic Crosstalk via PDGF/PDGFRβ and VCAM-1 Controls Angiotropism and Perivascular Positioning of Skeletal Progenitor Cells

(A) qRT-PCR of *PDGF-B* and *PDGF-D* in CD31$^+$ ECs (red bars; each sample consists of pooled sorted cells from 4–6 animals) and mOCL (6 or 7 days of spleen cell differentiation, gray bars, n = 3).

(B) Scratch assays with MC3T3 cells co-cultured with increasing amounts of HUVEC cells (n = 3) or HUVEC conditioned medium (CM) (n = 3–5); one-way ANOVA.

(C) Scratch assay of MC3T3 cells cultured with vehicle or HUVEC CM, with or without Imatinib, Orantinib or Amuvatinib, n = 3–6; one-way ANOVA.

(D) Endothelial tubule affinity assay, seeding osteogenic cells (green) on Matrigel-induced MS1 lattices (red) and quantifying cell attachment. ST2 and MC3T3 cells were pre-treated with vehicle or Imatinib. *PDGFRβ$^{(lox/lox)}$* mCV OBs were AdCre-/AdEmpty-transduced. Scale bar, 100 μm. n = 3 independent experiments (cell lines) or cell pools (primary cells), Student's t test.

(E) IHC of CD31 (red) at PFD7, Osx/GFP+ (green), nuclei (blue, hoechst); scale bar, 100 μm.

(F) Nearest neighbor distance between Osx/GFP+ cells and CD31$^+$ cells in control and PDGFRβ cKO calluses at PFD7; n = 3, Student's t test (left graph), two-way ANOVA (right).

(G) qRT-PCR of *PDGF-B* and *PDGF-D* in n = 5–6 calluses per time point. two-way ANOVA.

(H) *VCAM-1* qRT-PCR in *PDGFRβ$^{(lox/lox)}$* mCV OBs treated with AdCre or AdEmpty; n = 9; t test.

(I) Expression of *VCAM-1* in Osx/GFP+ OPCs and Col1/GFP+ OBs (RNA-seq); n = 3; *padj < 0.1.

(J) *VCAM-1* qRT-PCT in Osx/GFP$^+$ versus GFP$^-$ cells from E14.5 mice; n = 3; t test.

(K) qRT-PCR of *Itgα4* and *Itgβ1* in primary osteolineage cells (green bars), skeletal CD31$^+$ ECs (red bars), and mOCL (gray bar).

(L) IHC of VCAM-1 (red) in bone sections of (left) E15.5 Osx:Cre-GFP;IRG mice (Osx/GFP+ cells (green), nuclei (blue, hoechst); bars, 20 μm) and (right) 12-week-old mice stained for CD31 (green) (arrowheads, perivascular VCAM-1$^+$ cells; scale bars, 50 μm).

(M) Endothelial tubule affinity assay using control or VCAM-1 over-expressing (OE) MC3T3 cells. Scale bar, 100 μm. n = 3, t test.

(N) Cell-cell-adhesion assay of control and VCAM-1 OE cells to a MS1 monolayer, n = 5, t test.

Values, mean ± SEM. *p < 0.05, **p < 0.01, ***p < 0.001.

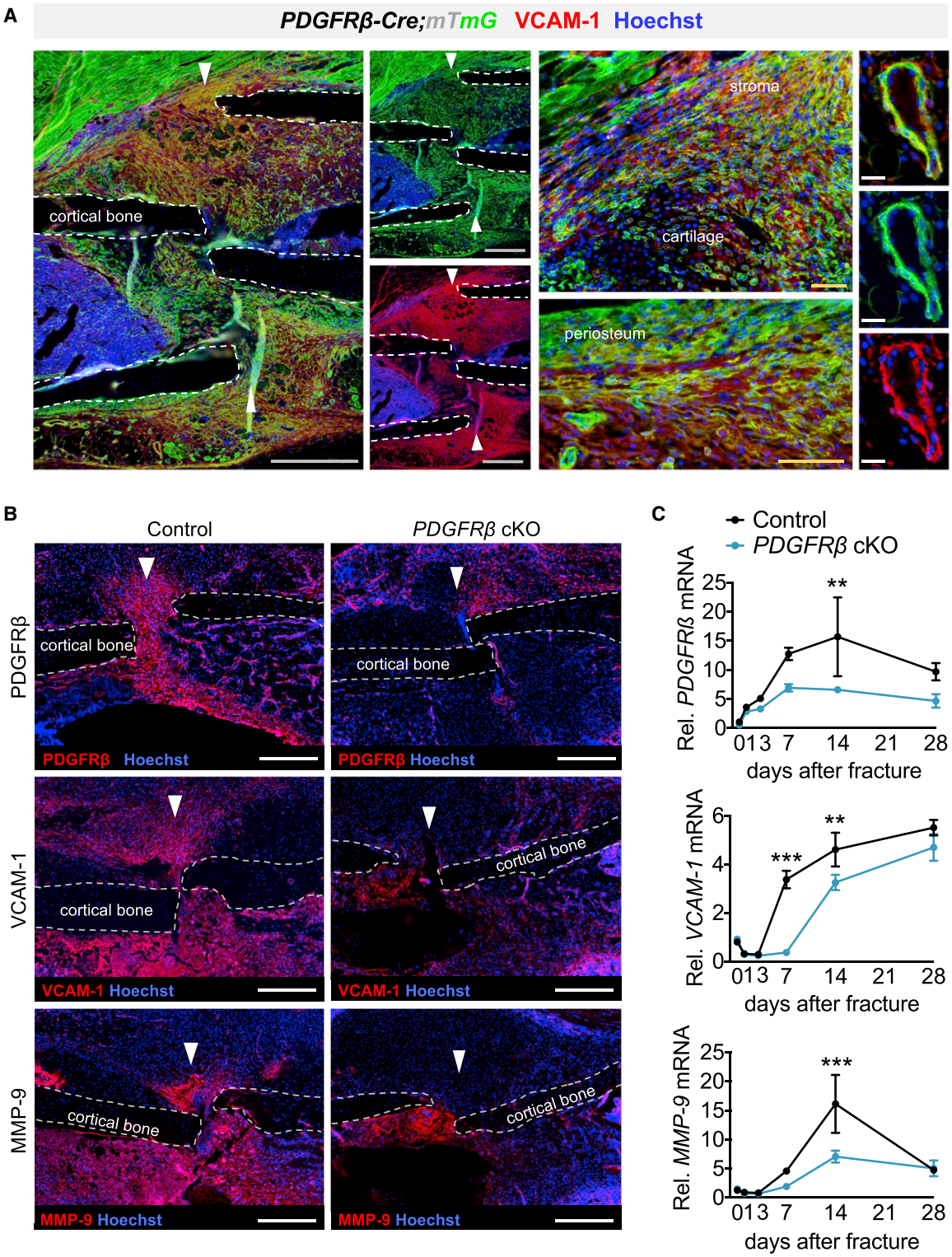

Figure 8. Impaired MMP-9 and VCAM-1 Induction during Bone Repair in PDGFRβ cKO Mice

(A) VCAM-1 IHC (red) in PDGFRβ-Cre;mTmG calluses at PFD7. Scale bars, 500 μm (gray), 50 μm (yellow), 20 μm (white).

(B) IHC for PDGFRβ, VCAM-1, and MMP-9 (red) in control and PDGFRβ cKO calluses at PFD7. Arrowheads, fracture site. Scale bar, 500 μm.

(C) qRT-PCR of *PDGFRβ*, *VCAM-1*, and *MMP-9* in calluses; n = 4–8; $^{**}p < 0.01$, $^{***}p < 0.001$ by two-way ANOVA; values, mean ± SEM.

appear to support a model in which endogenous repair mechanisms appeal broadly to diverse and heterogeneous SSC and/or SSPC subsets residing in the local environment of the injury, to orchestrate a common reparative response and ensure quick and successful mending of the defect. Speculatively, it may thus be that rather than rare, homogenous stem cells driving repair via a unidirectional downstream process of progressive lineage specification, the vast regenerative power of bone tissue may originate from the large activation potential, multi-lineage capacities and perhaps considerable plasticity among cell populations in the bone and BM environment in an acute reparative situation. PDGFRβ signaling may play a vital role in guiding the functional activation of such dynamic SSPC subsets.

Therapeutic Perspectives for Bone Regenerative Medicine

Each year millions of people suffer bone fractures, and this number is only expected to increase in the future with the growing incidence of osteoporosis-induced fractures, which often fail to heal. Advanced knowledge on the cell populations and signals mediating skeletal repair is essential to guide tissue engineering and cell therapy approaches for bone regeneration. We here started from the assumption that fetal Osx^+ OPCs could give insights into reparative SSPC behavior, since fracture healing recapitulates developmental programs (Gerstenfeld et al., 2003). Moreover, "developmental engineering" is considered a valuable route toward biology-based therapeutic interventions (Thompson et al., 2015). Similar to several BMPs (Tsuji et al., 2006), PlGF (Maes et al., 2006), and periostin (Duchamp de Lageneste et al., 2018), PDGFRβ was found critical for bone repair but dispensable for basal growth and homeostasis. A pathology-centered profile may render factors particularly suitable for therapeutic use, lowering the risks of side effects. Two FDA-approved rhPDGF-BB products are already used in clinical regenerative medicine, to treat chronic diabetic foot ulcers and bony defects resulting from advanced periodontal disease (DiGiovanni and Petricek, 2010). In the highly efficient repair model studied here, loss of PDGFRβ in SSPCs altered the healing process and exposed new regulatory mechanisms, but it did not block ultimate repair. Cortical bridging was achieved in both genotypes at post-fracture week 8, and the remaining callus volume and ossification was similar (data not shown). Still, our findings may stimulate further research into orthopedic applications based on the PDGF pathway, especially in more challenging repair systems such as those compromised by poor SSPC availability or revascularization potential, e.g., due to diabetes or advanced age. Pharmacological approaches were able to rescue diabetic SSC niche alterations before (Tevlin et al., 2017), and rhPDGF-BB-loaded scaffolds yielded encouraging results in rat models of diabetic and geriatric osteoporotic fracture healing (Hollinger et al., 2008). Of note, as PDGF-PDGFRβ signaling guides the delicate balancing of SSPC proliferation and differentiation, development of new pharmacological applications will need careful targeting, proper dosing, and effective timing to facilitate successful healing while avoiding a fibrotic outcome. Besides fibrosis, hyperactivity of PDGF has also been associated with atherosclerosis and cancer (Andrae et al., 2008). Thus, albeit highly promising, more research into the subtleties and applicability of the PDGF pathway is required now.

STAR★METHODS

Detailed methods are provided in the online version of this paper and include the following:

- KEY RESOURCES TABLE
- LEAD CONTACT AND MATERIALS AVAILABILITY
- EXPERIMENTAL MODEL AND SUBJECT DETAILS
  - Mouse Models
  - Fracture Model
  - Cell Lines and Primary Murine Bone Cells
- METHOD DETAILS
  - Analysis of Gene Expression
  - Bone Analysis by Micro-CT, Histology and IHC
  - Cell Cultures and *In Vitro* Assays
- QUANTIFICATION AND STATISTICAL ANALYSIS
- DATA AND CODE AVAILABILITY

SUPPLEMENTAL INFORMATION

Supplemental Information can be found online at https://doi.org/10.1016/j.devcel.2019.08.013.

ACKNOWLEDGMENTS

The authors thank D. Rowe, A. McMahon, H.M. Kronenberg, P. Carmeliet, and C. Lo Celso for sharing mouse models. We are grateful to SCEBP members D. Trompet, K. De Samblancx, M. Mesnieres, and G. Belmans for their expertise, support, and helpful discussions, and to the broader SBE with special thanks to F. Luyten, J. Peeters and A. Vandereijcken. A. Cortés Calabuig, V. Brys, S. Munck, and N. Corthout are greatly acknowledged for providing expertise on RNA-seq analysis and confocal imaging. We thank H. Kronenberg for critically commenting on the manuscript. This work was funded by grants to C.M. from the European Research Council under the European Union's Seventh Framework Programme (FP/2007–2013) (ERC grant agreement no. 282131), the Research Fund of the University of Leuven (KU Leuven OT/14/121), and the Research Foundation Flanders (FWO, #G0B5219N). A.-M.B. and M.V.H. were supported by FWO postdoctoral fellowships, N.D. by a doctoral fellowship of the Flemish government Agency for Innovation by Science and Technology (IWT), N.P. by the European Union's Horizon 2020 research and innovation program under Marie Sklodowska-Curie (MSCA-ITN grant agreement no. 721432) as Early Stage Researcher, and S.V. by a FWO PhD fellowship for Strategic Basic Research.

AUTHOR CONTRIBUTIONS

A.-M.B., N.D., R.J.T., N.P., E.N., R.C., and M.V.H. conducted all main experiments and analyzed data. A.-M.B., S.V., and K.T. performed the scRNA-seq experiment, with expertise and input from T.V. V.L. provided essential materials. All authors participated in designing experiments, interpreting, and discussing results. C.M. conceived the study and supervised the project. A.-M.B. and C.M. wrote the paper. All authors reviewed and edited the manuscript and approved the final version.

DECLARATION OF INTERESTS

The authors declare no competing interests.

Received: February 13, 2019
Revised: June 27, 2019
Accepted: August 21, 2019
Published: September 19, 2019

REFERENCES

Anders, S., Pyl, P.T., and Huber, W. (2015). HTSeq–a Python framework to work with high-throughput sequencing data. Bioinformatics *31*, 166–169.

Andrae, J., Gallini, R., and Betsholtz, C. (2008). Role of platelet-derived growth factors in physiology and medicine. Genes Dev. *22*, 1276–1312.

Armulik, A., Genové, G., and Betsholtz, C. (2011). Pericytes: developmental, physiological, and pathological perspectives, problems, and promises. Dev. Cell *21*, 193–215.

Bouletreau, P.J., Warren, S.M., Spector, J.A., Peled, Z.M., Gerrets, R.P., Greenwald, J.A., and Longaker, M.T. (2002). Hypoxia and VEGF up-regulate BMP-2 mRNA and protein expression in microvascular endothelial cells: implications for fracture healing. Plast. Reconstr. Surg *109*, 2384–2397.

Chan, C.K., Seo, E.Y., Chen, J.Y., Lo, D., McArdle, A., Sinha, R., Tevlin, R., Seita, J., Vincent-Tompkins, J., Wearda, T., et al. (2015). Identification and specification of the mouse skeletal stem cell. Cell *160*, 285–298.

Chan, C.K.F., Gulati, G.S., Sinha, R., Tompkins, J.V., Lopez, M., Carter, A.C., Ransom, R.C., Reinisch, A., Wearda, T., Murphy, M., et al. (2018). Identification of the human skeletal stem cell. Cell *175*, 43–56.

Colnot, C., Thompson, Z., Miclau, T., Werb, Z., and Helms, J.A. (2003). Altered fracture repair in the absence of MMP9. Development *130*, 4123–4133.

Cuttler, A.S., LeClair, R.J., Stohn, J.P., Wang, Q., Sorenson, C.M., Liaw, L., and Lindner, V. (2011). Characterization of Pdgfrb-Cre transgenic mice reveals reduction of ROSA26 reporter activity in remodeling arteries. Genesis *49*, 673–680.

De Gasperi, R., Rocher, A.B., Sosa, M.A., Wearne, S.L., Perez, G.M., Friedrich, V.L., Jr., Hof, P.R., and Elder, G.A. (2008). The IRG mouse: a two-color fluorescent reporter for assessing Cre-mediated recombination and imaging complex cellular relationships in situ. Genesis *46*, 308–317.

Debnath, S., Yallowitz, A.R., McCormick, J., Lalani, S., Zhang, T., Xu, R., Li, N., Liu, Y., Yang, Y.S., Eiseman, M., et al. (2018). Discovery of a periosteal stem cell mediating intramembranous bone formation. Nature *562*, 133–139.

Dejaeger, M., Böhm, A.M., Dirckx, N., Devriese, J., Nefyodova, E., Cardoen, R., St-Arnaud, R., Tournoy, J., Luyten, F.P., and Maes, C. (2017). Integrin-linked kinase regulates bone formation by controlling cytoskeletal organization and modulating BMP and Wnt signaling in osteoprogenitors. J. Bone Miner. Res. *32*, 2087–2102.

DiGiovanni, C.W., and Petricek, J.M. (2010). The evolution of rhPDGF-BB in musculoskeletal repair and its role in foot and ankle fusion surgery. Foot Ankle Clin *15*, 621–640.

Dirckx, N., Tower, R.J., Mercken, E.M., Vangoitsenhoven, R., Moreau-Triby, C., Breugelmans, T., Nefyodova, E., Cardoen, R., Mathieu, C., Van der Schueren, B., et al. (2018). Vhl deletion in osteoblasts boosts cellular glycolysis and improves global glucose metabolism. J. Clin. Invest *128*, 1087–1105.

Dirckx, N., Van Hul, M., and Maes, C. (2013). Osteoblast recruitment to sites of bone formation in skeletal development, homeostasis, and regeneration. Birth Defects Res. C Embryo Today *99*, 170–191.

Duchamp de Lageneste, O., Julien, A., Abou-Khalil, R., Frangi, G., Carvalho, C., Cagnard, N., Cordier, C., Conway, S.J., and Colnot, C. (2018). Periosteum contains skeletal stem cells with high bone regenerative potential controlled by Periostin. Nat. Commun *9*, 773.

Fiedler, J., Etzel, N., and Brenner, R.E. (2004). To go or not to go: migration of human mesenchymal progenitor cells stimulated by isoforms of PDGF. J. Cell. Biochem *93*, 990–998.

Garmy-Susini, B., Jin, H., Zhu, Y., Sung, R.J., Hwang, R., and Varner, J. (2005). Integrin alpha4beta1-VCAM-1-mediated adhesion between endothelial and mural cells is required for blood vessel maturation. J. Clin. Invest *115*, 1542–1551.

Gerstenfeld, L.C., Cullinane, D.M., Barnes, G.L., Graves, D.T., and Einhorn, T.A. (2003). Fracture healing as a post-natal developmental process: molecular, spatial, and temporal aspects of its regulation. J. Cell. Biochem *88*, 873–884.

He, X., Bougioukli, S., Ortega, B., Arevalo, E., Lieberman, J.R., and McMahon, A.P. (2017). Sox9 positive periosteal cells in fracture repair of the adult mammalian long bone. Bone *103*, 12–19.

Hellström, M., Kalén, M., Lindahl, P., Abramsson, A., and Betsholtz, C. (1999). Role of PDGF-B and PDGFR-beta in recruitment of vascular smooth muscle cells and pericytes during embryonic blood vessel formation in the mouse. Development *126*, 3047–3055.

Hollinger, J.O., Onikepe, A.O., MacKrell, J., Einhorn, T., Bradica, G., Lynch, S., and Hart, C.E. (2008). Accelerated fracture healing in the geriatric, osteoporotic rat with recombinant human platelet-derived growth factor-BB and an injectable beta-tricalcium phosphate/collagen matrix. J. Orthop. Res. *26*, 83–90.

Jacobsen, K.A., Al-Aql, Z.S., Wan, C., Fitch, J.L., Stapleton, S.N., Mason, Z.D., Cole, R.M., Gilbert, S.R., Clemens, T.L., Morgan, E.F., et al. (2008). Bone formation during distraction osteogenesis is dependent on both VEGFR1 and VEGFR2 signaling. J. Bone Miner. Res. *23*, 596–609.

Kalajzic, I., Kalajzic, Z., Kaliterna, M., Gronowicz, G., Clark, S.H., Lichtler, A.C., and Rowe, D. (2002). Use of type I collagen green fluorescent protein transgenes to identify subpopulations of cells at different stages of the osteoblast lineage. J. Bone Miner. Res. *17*, 15–25.

Kiselev, V.Y., Kirschner, K., Schaub, M.T., Andrews, T., Yiu, A., Chandra, T., Natarajan, K.N., Reik, W., Barahona, M., Green, A.R., et al. (2017). SC3: consensus clustering of single-cell RNA-seq data. Nat. Methods *14*, 483–486.

Kusumbe, A.P., Ramasamy, S.K., and Adams, R.H. (2014). Coupling of angiogenesis and osteogenesis by a specific vessel subtype in bone. Nature *507*, 323–328.

Lee, C.W., Lin, C.C., Lin, W.N., Liang, K.C., Luo, S.F., Wu, C.B., Wang, S.W., and Yang, C.M. (2007). TNF-alpha induces MMP-9 expression via activation of Src/EGFR, PDGFR/PI3K/Akt cascade and promotion of NF-kappaB/p300 binding in human tracheal smooth muscle cells. Am. J. Physiol. Lung Cell. Mol. Physiol. *292*, L799–L812.

Lindahl, P., Johansson, B.R., Levéen, P., and Betsholtz, C. (1997). Pericyte loss and microaneurysm formation in PDGF-B-deficient mice. Science *277*, 242–245.

Liu, Y., Strecker, S., Wang, L., Kronenberg, M.S., Wang, W., Rowe, D.W., and Maye, P. (2013). Osterix-cre labeled progenitor cells contribute to the formation and maintenance of the bone marrow stroma. PLoS One *8*, e71318.

Madisen, L., Zwingman, T.A., Sunkin, S.M., Oh, S.W., Zariwala, H.A., Gu, H., Ng, L.L., Palmiter, R.D., Hawrylycz, M.J., Jones, A.R., et al. (2010). A robust and high-throughput Cre reporting and characterization system for the whole mouse brain. Nat. Neurosci. *13*, 133–140.

Maes, C., Carmeliet, G., and Schipani, E. (2012). Hypoxia-driven pathways in bone development, regeneration and disease. Nat. Rev. Rheumatol. *8*, 358–366.

Maes, C., Coenegrachts, L., Stockmans, I., Daci, E., Luttun, A., Petryk, A., Gopalakrishnan, R., Moermans, K., Smets, N., Verfaillie, C.M., et al. (2006). Placental growth factor mediates mesenchymal cell development, cartilage turnover, and bone remodeling during fracture repair. J. Clin. Invest. *116*, 1230–1242.

Maes, C., Kobayashi, T., Selig, M.K., Torrekens, S., Roth, S.I., Mackem, S., Carmeliet, G., and Kronenberg, H.M. (2010). Osteoblast precursors, but not mature osteoblasts, move into developing and fractured bones along with invading blood vessels. Dev. Cell *19*, 329–344.

Marecic, O., Tevlin, R., McArdle, A., Seo, E.Y., Wearda, T., Duldulao, C., Walmsley, G.G., Nguyen, A., Weissman, I.L., Chan, C.K., et al. (2015). Identification and characterization of an injury-induced skeletal progenitor. Proc. Natl. Acad. Sci. USA *112*, 9920–9925.

Matthews, B.G., Grcevic, D., Wang, L., Hagiwara, Y., Roguljic, H., Joshi, P., Shin, D.G., Adams, D.J., and Kalajzic, I. (2014). Analysis of alphaSMA-labeled progenitor cell commitment identifies notch signaling as an important pathway in fracture healing. J. Bone Miner. Res. *29*, 1283–1294.

Maye, P., Fu, Y., Butler, D.L., Chokalingam, K., Liu, Y., Floret, J., Stover, M.L., Wenstrup, R., Jiang, X., Gooch, C., et al. (2011). Generation and characterization of Col10a1-mcherry reporter mice. Genesis *49*, 410–418.

McCarthy, D.J., Campbell, K.R., Lun, A.T., and Wills, Q.F. (2017). Scater: pre-processing, quality control, normalization and visualization of single-cell RNA-seq data in R. Bioinformatics *33*, 1179–1186.

McClelland, P., Onyia, J.E., Miles, R.R., Tu, Y., Liang, J., Harvey, A.K., Chandrasekhar, S., Hock, J.M., and Bidwell, J.P. (1998). Intermittent administration of parathyroid hormone (1–34) stimulates matrix metalloproteinase-9 (MMP-9) expression in rat long bone. J. Cell. Biochem *70*, 391–401.

Méndez-Ferrer, S., Michurina, T.V., Ferraro, F., Mazloom, A.R., Macarthur, B.D., Lira, S.A., Scadden, D.T., Ma'ayan, A., Enikolopov, G.N., and Frenette, P.S. (2010). Mesenchymal and haematopoietic stem cells form a unique bone marrow niche. Nature *466*, 829–834.

Mizoguchi, T., Pinho, S., Ahmed, J., Kunisaki, Y., Hanoun, M., Mendelson, A., Ono, N., Kronenberg, H.M., and Frenette, P.S. (2014). Osterix marks distinct waves of primitive and definitive stromal progenitors during bone marrow development. Dev. Cell *29*, 340–349.

Morikawa, S., Mabuchi, Y., Kubota, Y., Nagai, Y., Niibe, K., Hiratsu, E., Suzuki, S., Miyauchi-Hara, C., Nagoshi, N., Sunabori, T., et al. (2009). Prospective identification, isolation, and systemic transplantation of multipotent mesenchymal stem cells in murine bone marrow. J. Exp. Med *206*, 2483–2496.

Muzumdar, M.D., Tasic, B., Miyamichi, K., Li, L., and Luo, L. (2007). A global double-fluorescent Cre reporter mouse. Genesis *45*, 593–605.

Omatsu, Y., Sugiyama, T., Kohara, H., Kondoh, G., Fujii, N., Kohno, K., and Nagasawa, T. (2010). The essential functions of adipo-osteogenic progenitors as the hematopoietic stem and progenitor cell niche. Immunity *33*, 387–399.

Ono, N., Ono, W., Mizoguchi, T., Nagasawa, T., Frenette, P.S., and Kronenberg, H.M. (2014a). Vasculature-associated cells expressing nestin in developing bones encompass early cells in the osteoblast and endothelial lineage. Dev. Cell *29*, 330–339.

Ono, N., Ono, W., Nagasawa, T., and Kronenberg, H.M. (2014b). A subset of chondrogenic cells provides early mesenchymal progenitors in growing bones. Nat. Cell Biol. *16*, 1157–1167.

Ozaki, Y., Nishimura, M., Sekiya, K., Suehiro, F., Kanawa, M., Nikawa, H., Hamada, T., and Kato, Y. (2007). Comprehensive analysis of chemotactic factors for bone marrow mesenchymal stem cells. Stem Cells Dev. *16*, 119–129.

Park, D., Spencer, J.A., Koh, B.I., Kobayashi, T., Fujisaki, J., Clemens, T.L., Lin, C.P., Kronenberg, H.M., and Scadden, D.T. (2012). Endogenous bone marrow MSCs are dynamic, fate-restricted participants in bone maintenance and regeneration. Cell Stem Cell *10*, 259–272.

Rodda, S.J., and McMahon, A.P. (2006). Distinct roles for Hedgehog and canonical Wnt signaling in specification, differentiation and maintenance of osteoblast progenitors. Development *133*, 3231–3244.

Romeo, S.G., Alawi, K.M., Rodrigues, J., Singh, A., Kusumbe, A.P., and Ramasamy, S.K. (2019). Endothelial proteolytic activity and interaction with non-resorbing osteoclasts mediate bone elongation. Nat. Cell Biol. *21*, 430–441.

Sacchetti, B., Funari, A., Michienzi, S., DiCesare, S., Piersanti, S., Saggio, I., Tagliafico, E., Ferrari, S., Robey, P.G., Riminucci, M., et al. (2007). Self-renewing osteoprogenitors in bone marrow sinusoids can organize a hematopoietic microenvironment. Cell *131*, 324–336.

Salazar, V.S., Gamer, L.W., and Rosen, V. (2016). BMP signalling in skeletal development, disease and repair. Nat. Rev. Endocrinol. *12*, 203–221.

Schipani, E., Maes, C., Carmeliet, G., and Semenza, G.L. (2009). Regulation of osteogenesis-angiogenesis coupling by HIFs and VEGF. J. Bone Miner. Res. *24*, 1347–1353.

Schito, L., Rey, S., Tafani, M., Zhang, H., Wong, C.C., Russo, A., Russo, M.A., and Semenza, G.L. (2012). Hypoxia-inducible factor 1-dependent expression of platelet-derived growth factor B promotes lymphatic metastasis of hypoxic breast cancer cells. Proc. Natl. Acad. Sci. USA *109*, E2707–E2716.

Schmahl, J., Rizzolo, K., and Soriano, P. (2008). The PDGF signaling pathway controls multiple steroid-producing lineages. Genes Dev. *22*, 3255–3267.

Shi, Y., He, G., Lee, W.C., McKenzie, J.A., Silva, M.J., and Long, F. (2017). Gli1 identifies osteogenic progenitors for bone formation and fracture repair. Nat. Commun *8*, 2043.

Subramanian, A., Tamayo, P., Mootha, V.K., Mukherjee, S., Ebert, B.L., Gillette, M.A., Paulovich, A., Pomeroy, S.L., Golub, T.R., Lander, E.S., et al. (2005). Gene set enrichment analysis: a knowledge-based approach for interpreting genome-wide expression profiles. Proc. Natl. Acad. Sci. USA *102*, 15545–15550.

Tang, Y., Wu, X., Lei, W., Pang, L., Wan, C., Shi, Z., Zhao, L., Nagy, T.R., Peng, X., Hu, J., et al. (2009). TGF-beta1-induced migration of bone mesenchymal stem cells couples bone resorption with formation. Nat. Med *15*, 757–765.

Tevlin, R., Seo, E.Y., Marecic, O., McArdle, A., Tong, X., Zimdahl, B., Malkovskiy, A., Sinha, R., Gulati, G., Li, X., et al. (2017). Pharmacological rescue of diabetic skeletal stem cell niches. Sci. Transl. Med. *9*.

Thompson, E.M., Matsiko, A., Farrell, E., Kelly, D.J., and O'Brien, F.J. (2015). Recapitulating endochondral ossification: a promising route to in vivo bone regeneration. J. Tissue Eng. Regen. Med. *9*, 889–902.

Tsuji, K., Bandyopadhyay, A., Harfe, B.D., Cox, K., Kakar, S., Gerstenfeld, L., Einhorn, T., Tabin, C.J., and Rosen, V. (2006). BMP2 activity, although dispensable for bone formation, is required for the initiation of fracture healing. Nat. Genet. *38*, 1424–1429.

van Gastel, N., Stegen, S., Stockmans, I., Moermans, K., Schrooten, J., Graf, D., Luyten, F.P., and Carmeliet, G. (2014). Expansion of murine periosteal progenitor cells with fibroblast growth factor 2 reveals an intrinsic endochondral ossification program mediated by bone morphogenetic protein 2. Stem Cells *32*, 2407–2418.

Vu, T.H., Shipley, J.M., Bergers, G., Berger, J.E., Helms, J.A., Hanahan, D., Shapiro, S.D., Senior, R.M., and Werb, Z. (1998). MMP-9/gelatinase B is a key regulator of growth plate angiogenesis and apoptosis of hypertrophic chondrocytes. Cell *93*, 411–422.

Wang, X., Yu, Y.Y., Lieu, S., Yang, F., Lang, J., Lu, C., Werb, Z., Hu, D., Miclau, T., Marcucio, R., et al. (2013). MMP9 regulates the cellular response to inflammation after skeletal injury. Bone *52*, 111–119.

Wang, Y., Wan, C., Deng, L., Liu, X., Cao, X., Gilbert, S.R., Bouxsein, M.L., Faugere, M.C., Guldberg, R.E., Gerstenfeld, L.C., et al. (2007). The hypoxia-inducible factor alpha pathway couples angiogenesis to osteogenesis during skeletal development. J. Clin. Invest *117*, 1616–1626.

Worthley, D.L., Churchill, M., Compton, J.T., Tailor, Y., Rao, M., Si, Y., Levin, D., Schwartz, M.G., Uygur, A., Hayakawa, Y., et al. (2015). Gremlin 1 identifies a skeletal stem cell with bone, cartilage, and reticular stromal potential. Cell *160*, 269–284.

Wuidart, A., Sifrim, A., Fioramonti, M., Matsumura, S., Brisebarre, A., Brown, D., Centonze, A., Dannau, A., Dubois, C., Van Keymeulen, A., et al. (2018). Early lineage segregation of multipotent embryonic mammary gland progenitors. Nat. Cell Biol. *20*, 666–676.

Xie, H., Cui, Z., Wang, L., Xia, Z., Hu, Y., Xian, L., Li, C., Xie, L., Crane, J., Wan, M., et al. (2014). PDGF-BB secreted by preosteoclasts induces angiogenesis during coupling with osteogenesis. Nat. Med *20*, 1270–1278.

Yellowley, C. (2013). CXCL12/CXCR4 signaling and other recruitment and homing pathways in fracture repair. Bonekey Rep *2*, 300.

Zaidi, M. (2007). Skeletal remodeling in health and disease. Nat. Med *13*, 791–801.

Zhou, B.O., Yue, R., Murphy, M.M., Peyer, J.G., and Morrison, S.J. (2014). Leptin-receptor-expressing mesenchymal stromal cells represent the main source of bone formed by adult bone marrow. Cell Stem Cell *15*, 154–168.

STAR★METHODS

KEY RESOURCES TABLE

REAGENT or RESOURCE	SOURCE	IDENTIFIER
Antibodies		
CD31 Rat Anti-Mouse, PE-Cyanine7 (FACS)	eBioscience	Cat#25031181; RRID: AB_2734962
CD51 Rat Anti-Mouse, PE	eBioscience	Cat#12051283; RRID: AB_465705
Chicken Polyclonal Anti-GFP	Abcam	Cat#ab13970; RRID: AB_300798
Goat Polyclonal Anti-CD31 (IHC)	R&D Systems	Cat#AF3628; RRID: AB_2161028
Goat Polyclonal Anti-MMP-9	R&D Systems	Cat#AF909; RRID: AB_355706
Goat Polyclonal Anti-PDGFRβ	Santa Cruz Biotechnology	Cat#SC-1627; RRID: AB_631067
Normal Goat IgG Control	R&D Systems	Cat#AB-108-C; RRID: AB_354267
PerCP/Cyanine5.5 Anti-Mouse CD45	Biolegend	Cat#103132; RRID: AB_893340
PerCP/Cyanine5.5 Anti-Mouse TER119	Biolegend	Cat#116227; RRID: AB_893638
Rabbit Monoclonal Anti-VCAM-1	Cell Signaling Technology	Cat#39036; RRID: AB_2799146
Rat Monoclonal Anti-BrdU	Novus	Cat#NB500169; RRID: AB_10002608
Rat Monoclonal Anti-CD31 (IHC)	BD Pharmingen	Cat#550274; RRID: AB_393571
Rat Monoclonal Anti-Endomucin (Emcn)	Santa Cruz Biotechnology	Cat#SC65495; RRID: AB_2100037
Alexa Fluor 546 Donkey-Anti-Goat	Thermo Fisher Scientific	Cat#A11056; RRID: AB_2534103
Alexa Fluor 546 Donkey-Anti-Rabbit	Thermo Fisher Scientific	Cat#A10040; RRID: AB_2534016
Alexa Fluor 546 Goat-Anti-Rabbit	Thermo Fisher Scientific	Cat#A11071; RRID: AB_2534115
Alexa Fluor 647 Goat-Anti-Rabbit	Thermo Fisher Scientific	Cat#A21245; RRID: AB_2535813
Biotin Polyclonal Goat-Anti-Rat	BD Biosciences	Cat#5554014; RRID: AB_395209
Donkey-Anti-Goat IgG H&L DyLight 647	Abcam	Cat#ab150131; RRID: AB_2732857
Goat-Anti-Chicken IgY H&L DyLight 488	Abcam	Cat#ab96951; RRID: AB_10679800
Goat-Anti-Rat IgG Fc DyLight 550	Abcam	Cat#ab96972; RRID: AB_10679833
Virus Strains		
Ad5CMVcre	Viral Vector Core	https://medicine.uiowa.edu/vectorcore/
Ad5CMVempty	Viral Vector Core	https://medicine.uiowa.edu/vectorcore/
Chemicals, Peptides, and Recombinant Proteins		
5-bromo-2′-desoxirudine (BrdU) (*in vitro* use)	Roche	Cat#11647229
5-bromo-2′-desoxirudine (BrdU) (*in vivo* use)	Sigma-Aldrich	Cat#10280879001
7-AAD Viability Staining Solution	Thermo Fisher Scientific	Cat#00699350
Alexa Fluor 488 Phalloidin	Thermo Fisher Scientific	Cat#A12379
Alizarin Red S	Sigma-Aldrich	Cat#A3757
Amuvatinib (MP-470)	Seleckchem	Cat#S1244
Antibiotic-Antimycotic (100x)	Thermo Fisher Scientific	Cat#15240062
b-Glycerophosphate Disodium Salt Hydrate	Sigma-Aldrich	Cat#251291
Calcein	Sigma-Aldrich	Cat#C0875
CD31 Microbeads	Milteny Biotec	Cat#130-097-418
CD45 Microbeads	Milteny Biotec	Cat#130-097-153
Collagen I High Concentration, Rat Tail	Corning	Cat#354249
Collagenase Type II	Thermo Fisher Scientific	Cat#17101015
Direct Red 80 (Sirius Red)	Sigma-Aldrich	Cat#365548
Dispase	Thermo Fisher Scientific	Cat#17105041
dNTP Set 100-mM Solutions	Thermo Fisher Scientific	Cat#R0181

(*Continued on next page*)

Continued

REAGENT or RESOURCE	SOURCE	IDENTIFIER
Donkey Serum	Sigma-Aldrich	Cat#S30
EGM-2 Endothelial Cell Growth Medium-2	Lonza	Cat#CC3162
External RNA Controls Consortium Spike-In Mixture A	Thermo Fisher Scientific	Cat#4456740
Fast Red Violet LB	Sigma-Aldrich	Cat#F3381
Freeze Gel Q Path	VWR International	Cat#07111245
G-418 Solution	Roche	Cat#04727878001
Gelatin from Porcine Skin	Sigma-Aldrich	Cat#G6144
Gelatin Solution	Sigma-Aldrich	Cat#G1393
Goat Serum	Sigma-Aldrich	Cat#G9023
Goat Serum	Dako	Cat#X090710
HyClone Fetal Bovine Serum	GE Heathcare Life Sciences	Cat#SV30160.03
Imatinib (PDGFRβ Inhibitor)	Seleckchem	Cat#S2475
JNJ 0966	R&D Systems	Cat#6439
Ketamine	EuroVet	Cat#804132
Lipofectamine 2000	Thermo Fisher Scientific	Cat#11668027
Matrigel	Corning	Cat#356231
Mitomycin	Sigma-Aldrich	Cat#M0503
MMP-9 Inhibitor I	Merck Millipore	Cat#444278
Naphthol AS-MX Phosphate	Sigma-Aldrich	Cat#855
OPTIMEM	Thermo Fisher Scientific	Cat#31985
Orantinib (TSU-68, SU6668)	Seleckchem	Cat#S1470
pCMV-Entry Tagged Cloning Vector	OriGene	Cat#PS100001
Perifosine (AKT Inhibitor)	Seleckchem	Cat#S1037
Random Primers	Thermo Fisher Scientific	Cat#48190011
Recombinant Human PDGF-BB	R&D Systems	Cat#220BB
Recombinant Human PDGF-DD	R&D Systems	Cat#1159SB
Recombinant Human VEGF 165	R&D Systems	Cat#293VE
Recombinant Mouse M-CSF	R&D Systems	Cat#416ML010/CF
Recombinant Mouse RANKL	R&D Systems	Cat#462TEC010/CF
RO5126766 (RAF/MEK Inhibitor)	Seleckchem	Cat#S7170
SCH772984 (ERK1/2 Inhibitor)	Seleckchem	Cat#7101
Ultra Pure LMP Agarose (Low Melting Point)	Thermo Fisher Scientific	Cat#16520-050
Vcam1(NM-011693) Mouse cDNA Clone	OriGene	Cat#MC221229
Vybrant DiI-Labeling Solution	Thermo Fisher Scientific	Cat#V22885
Vybrant DiO-Labeling Solution	Thermo Fisher Scientific	Cat#V22886
Wortmannin (PI3K Inhibitor)	Seleckchem	Cat#S2758
Xylazine	VMD	Cat#E007380310
Vetergesic	Ecuphar	Cat#2623-627
Critical Commercial Assays		
DNA 1000 Kit	Agilent Technologies	Cat#5067-1504
Click-iT™ EdU Alexa Fluor™ 647 Imaging Kit	Thermo Fisher Scientific	Cat#C10340
Fast SYBR Green Master Mix	Thermo Fisher Scientific	Cat#4385612
RNeasy Micro Kit	Qiagen	Cat#74004
RNeasy Mini Kit	Qiagen	Cat#74106
SuperScript II Reverse Transcriptase	Thermo Fisher Scientific	Cat#18064014
TaqMan Fast Universal PCR Master Mix	Applied Biosystems	Cat#4352042

(*Continued on next page*)

Continued

REAGENT or RESOURCE	SOURCE	IDENTIFIER
TruSeq Stranded Total RNA Library Prep	Illumina	Cat#2002097
TSA Cyanine 3 System	PerkinElmer	Cat#NEL704A001KT
TSA Cyanine 5 System	PerkinElmer	Cat#NEL705A001KT
TSA Indirect System	PerkinElmer	Cat#NEL700001KT
Deposited Data		
Bulk RNA Seq Database	European Nucleotide Archive (ENA)	Study accession number ENA: PRJEB33441
Single Cell RNA Seq Database	European Nucleotide Archive (ENA)	Study accession number ENA: PRJEB33444
Experimental Models: Cell Lines		
Human: HUVEC	Lonza	Cat #C2519AS
Mouse: MC3T3-E1	Riken BRC Cell Bank	Cat #RCB1126
Mouse: MS1 (Mile SVEN 1)	ATCC	Cat #CRL-2279
Mouse: ST2	Riken BRC Cell Bank	Cat #RCB0224
Experimental Models: Organisms/Strains		
Mouse: 'Crl:CD1(CRL)'	Charles River Laboratories	
Mouse: Col1(2.3Kb)-GFP	David Rowe, University of Connecticut Health Center	Kalajzic et al., 2002
Mouse: 'ColX-mCherry': Tg(Col10a1-mCherry)3Pmay	Jackson Laboratory (origin: Peter Maye, University of Connecticut Health Center)	JAX Stock No: 017465 (Maye et al., 2011)
Mouse: 'IRG': B6.Cg-Tg(CAG-DsRed,-EGFP)5Gae/J	Jackson Laboratory (origin: Gregory Elder, James J. Peters VA Medical Center)	JAX Stock No: 008705 (De Gasperi et al., 2008)
Mouse: 'mTmG': B6.129(Cg)-Gt(ROSA)26Sortm4(ACTB-tdTomato,-EGFP)Luo/J	Jackson Laboratory (origin: Liqun Luo, Stanford University)	JAX Stock No: 007676 (Muzumdar et al., 2007)
Mouse: 'Osx-Cre:GFP': B6.Cg-Tg(Sp7-tTA,tetO-EGFP/cre)1Amc/J	Andrew McMahon, University of Southern California	Rodda and McMahon, 2006
Mouse: Osx-CreERT	Henry Kronenberg, Massachusetts General Hospital	Maes et al., 2010
Mouse: PDGFRβ-Cre	Volkhard Lindner, Maine Medical Center	Cuttler et al., 2011
Mouse: 'PDGFRβ(flox)': 129S4/SvJae-Pdgfrb$^{tm11Sor/J}$	Jackson Laboratory (origin: Philippe Soriano, Mount Sinai School of Medicine)	JAX Stock No: 010977 (Schmahl et al., 2008)
Mouse: 'tdTomato': Ai9(RLC-tdT): B6.Cg-Gt(ROSA)26Sortm9(CAG-tdTomato)Hze/J	Jackson Laboratory (origin: Hongkui Zeng, Allen Institute for Brain Science	JAX Stock No: 007909 (Madisen et al., 2010)
Oligonucleotides		
Table S3, for oligonucleotides		
Software and Algorithms		
Cellsense		Olympus
CTAn, CTVol		Bruker
DeSeq, EdgeR and Cufflinks 2.2.1		Bioconductor: https://bioconductor.org
Cuffquant (Cufflinks 2.2.1)		Cole Trapnell Lab: http://cole-trapnell-lab.github.io/cufflinks/getting_started/
Cutadapt 1.13		https://cutadapt.readthedocs.io/en/stable/index.html
DeSeq		Bioconductor: https://bioconductor.org
ggplot2 (Version 3.0.0)		https://www.tidyverse.org/articles/2018/07/ggplot2-3-0-0/

(*Continued on next page*)

Continued

REAGENT or RESOURCE	SOURCE	IDENTIFIER
GSEA (MSigDBv6,)		Broad Institute: http://www.gsea-msigdb.org/gsea/index.jsp
NIS-Elements		Nikon
HT-Seq Count v0.5.3p3		SoureForge: https://sourceforge.net/projects/htseq/
HTSeq (Version 0.6.0)		https://htseq.readthedocs.io/en/release_0.9.1/history.html
ImageJ 1.52A		NIH: https://imagej.nih.gov/ij/download.html
Nrecon		Bruker
OsteoMeasure		OsteoMetrics
Pheatmap (Version 1.0.10)		https://cran.r-project.org/web/packages/pheatmap/index.html
Prism 6		Graphpad Software: www.graphpad.com
Python v3.6		Python software foundation
R v3.5.1 (CRAN)		https://cran.r-project.org
SAMtools v0.1.19.24		http://samtools.sourceforge.net
SC3 (Version 1.8.0)		http://packages.renjin.org/package/org.renjin.bioconductor/SC3
Scater (Version 1.8.0)		http://bioconductor.org/packages/release/bioc/html/scater.html
Scran (Version 1.8.2)		http://packages.renjin.org/package/org.renjin.bioconductor/scran
STAR		https://github.com/alexdobin/STAR
TopHat v2.0.13		John Hopkins University: https://ccb.jhu.edu/software/tophat/index.shtml

LEAD CONTACT AND MATERIALS AVAILABILITY

Further information and requests for resources and reagents should be directed to and will be fulfilled by the Lead Contact, Christa Maes (christa.maes@kuleuven.be). This study did not generate new unique reagents.

EXPERIMENTAL MODEL AND SUBJECT DETAILS

Mouse Models

Animal Housing and General Procedures

All animals were housed in a temperature and humidity-controlled environment, with a 12 h light/dark cycle, and access to food and water *ad libitum*. Animal experiments and care were performed in accordance with the guidelines of institutional authorities and formally approved by the Animal Ethics Committee of the KU Leuven. The sources of all genetically modified mouse strains used in this study are provided in the Key Resources Table.

For analysis of cell proliferation, mice were injected with 100 mg/kg body weight (BW) bromodeoxyuridine (BrdU) or 10 mg/kg BW 5-ethynyl-2'-deoxyuridine (EdU) 3 h prior to sacrifice. Mice that were to be subjected to dynamic histomorphometry received two i.p. injections of 20 mg/kg calcein (Sigma), at 4 days and 1 day prior to sacrifice.

Mice used to investigate bone development, physiological bone growth and homeostasis were harvested by cesarean section at the indicated fetal stage (E14.5-E16.5) or euthanized at the age indicated in the respective figure legends (early postnatal mice at P10; juvenile mice at 4-5 weeks of age; young adult mice at 12-13 weeks).

For breeding and for experiments in which only wild type mice were used, CD-1(CRL) mice were purchased from Charles River Laboratories.

Mice for osteolineage molecular profiling

For molecular profiling of primary Osx^{+} OPCs and Col1^{+} OBs by RNA-Seq, Osx-Cre:GFP (Rodda and McMahon, 2006) and Col1a1(2.3kb)-GFP (Kalajzic et al., 2002) mice were subjected to 10 alternating inter- and back-cross cycles (using CD1 mice) to obtain genetically closely related mice in the CD1 background. Osx-Cre:GFP and Col1a1(2.3kb)-GFP mice were genotyped for the Cre or GFP transgene, respectively, using genotyping primers listed in Table S3 (oligonucleotides). To optimize the perichondrial

digest protocol (see Figure S1A), Osx-Cre:GFP mice were crossed to ColX-mCherry mice (Maye et al., 2011) to obtain Osx-Cre:GFP/ColX-mCherry double positive offspring. Those were identified microscopically based on GFP and mCherry fluorescence.

PDGFRβ conditional knockout (cKO) mice

Mice in which the PDGFRβ gene was inactivated in Osx$^+$ cells and their descendants, were generated by crossing 129S4/SvJae-Pdgfrb$^{tm11Sor/J}$ mice carrying loxP sites about 500 bp upstream of and 2,100 bp downstream from the exons encoding the first and second immunoglobulin domain, respectively (Schmahl et al., 2008), with Osx-Cre:GFP mice expressing Cre as a fusion protein with GFP under the control of the osterix (*Osx*, *Sp7*) promoter (Rodda and McMahon, 2006). The animals were bred on a mixed genetic background and genotyping for Cre and the PDGFRβ alleles was performed by PCR as described (Maes et al., 2010; Schmahl et al., 2008) using the primers listed in Table S3. Throughout the study, PDGFRβ cKO [Osx-Cre:GFP(Tg);PDGFRβ$^{(lox/lox)}$] mice were compared to Control [Osx-Cre:GFP(Tg);PDGFRβ$^{(+/+)}$] mice, essentially littermates, expressing the Osx-Cre:GFP transgene. To visualize targeted cells (in Figure S3B), a single copy of the tdTomato (tdTom) Ai9 transgene (Madisen et al., 2010) was crossed into this mouse line to obtain Osx-Cre:GFP(Tg);PDGFRβ$^{(lox/lox)}$;tdTom(Tg) and Osx-Cre:GFP(Tg);PDGFRβ$^{(+/+)}$;tdTom(Tg) mice. Mice were genotyped for the tdTom transgene using the primers listed in Table S3.

Mice used for Osx$^+$ or PDGFRβ$^+$ lineage mapping

Visualization of Osx- or PDGFRβ-expressing cells and their respective progeny was conducted by crossing male Osx-Cre:GFP (Rodda and McMahon, 2006) or PDGFRβ-Cre (Cuttler et al., 2011) transgenic mice with females homozygous for the (i) mTmG (Muzumdar et al., 2007) or (ii) IRG (inducible Red and Green) reporter transgene (De Gasperi et al., 2008). (i) Osx-Cre:GFP(Tg);mTmG(Tg) and PDGFRβ-Cre;mTmG(Tg) offspring carried a single copy of the mTmG reporter expressing a modified membranous version of the red fluorescent protein tdTom under normal conditions, until Cre-recombination results in excision of the stop cassette in the transgene leading to a switch from tdTom-expression to expression of a membranous form of GFP (denoted as mG+ cells). (ii) Osx-Cre:GFP(Tg);IRG(Tg) offspring carried a single copy of the IRG reporter. These mice ubiquitously expressed DsRed-Express, a red fluorescent protein (RFP) in the absence of Cre-mediated recombination, and an enhanced green fluorescent protein (EGFP) following recombination. The presence of the IRG transgene was assessed microscopically based on the fluorescent signal.

Mice used for Osx+ lineage tracing

For lineage tracing of Osx$^+$ cells, OsxCreERT (Maes et al., 2010) male mice in mixed genetic background where bred to females homozygous for the tdTom Ai9 reporter transgene (Madisen et al., 2010) to obtain OsxCreERT(Tg/+);tdTom(Tg/+) offspring. At E14.5, pregnant females received 2 mg tamoxifen i.p.; P5 pups were injected i.p. with 50μl tamoxifen at a concentration of 2 mg/mL. Tamoxifen-induced Cre-activity in Osx-CreERT(Tg) offspring resulted in the excision of the floxed stop cassette upstream of the tdTom transgene, leading to tdTom expression in all Osx-CreERT-expressing cells and their descendants. OsxCreERT;tdTom mice were genotyped for the Cre and tdTom transgene using genotyping primers listed in Table S3 (oligonucleotides).

Fracture Model

10- to 12-week-old mice were anesthetized with i.p. injections of 100 mg/kg ketamine (EuroVet) and 10 mg/kg xylazine (VMD). Muscles were moved down at the tibial crest using a 25G needle to avoid extensive muscle damage during the fracture procedure. Tibia fractures were made ~2mm distal to the growth plate using a Comet diamant saw Miniflex (diameter 6.5mm) and fixed using a 27G needle inserted into the medullary cavity through the proximal tibia and extending beyond the fracture site into the distal diaphysis. Following the surgery, the mice were sutured and s.c. injected with 3μg of Vetergesic (Ecuphar). Detailed descriptions of the surgical procedure and healing process in this murine semi-stabilized tibia fracture model can be found in (Maes et al., 2006, 2010).

Cell Lines and Primary Murine Bone Cells

Osteoblastic MC3T3-E1 and mesenchymal ST2 cell lines (see Key Resources Table for sources) were grown in Minimum Essential Media alpha (αMEM; Thermo Fisher Scientific) supplemented with 10% HyClone Fetal Bovine Serum (FBS) (GE Heathcare Life Sciences) and 1% Antibiotic-Antimycotic (AA) (Thermo Fisher Scientific). Human umbilical vein endothelial cells (HUVECs) were obtained from Lonza and grown in Endothelial Cell Growth Medium-2 (EGM-2) BulletKit media (Lonza) supplemented with 1% AA and used at passage 2 to 5. Mouse-derived MS1 cells were cultured in Dulbecco's Minimum Essential Media (DMEM; Thermo Fisher Scientific) supplemented with 5% FBS and 1% AA.

Primary murine calvaria-derived osteoblasts (mCV OBs) were isolated from calvaria of newborn mice (P1-3). Murine bone marrow-derived stromal cells (mBMSCs) were derived from 3-week-old or 6-8-week-old mice and murine periosteal cells (mPDCs) were derived from long bones of 6-8-week-old mice. Primary long bone-derived murine osteoblasts (mOBs) were isolated from 3-week-old mice or from fracture calluses at PFD10. Primary murine endothelial cells (mECs) were isolated based on CD31 marker expression, from fetal, adult, or fractured bones, by MACS or FACS. Primary murine osteoclasts (mOCLs) were differentiated *in vitro* from spleen cells of 12-week-old mice by adding recombinant mouse (rm)RANKL (R&D Systems) and rmM-CSF (R&D Systems) to the culture medium. Primary cell isolation and culture conditions are described in detail below. Primary cells were derived from male and female mice of CD1 or mixed genetic background, housed in standard conditions as described above ('Mouse models').

Cell lines and primary cells were cultured at 37°C with 5% CO2.

METHOD DETAILS

Analysis of Gene Expression

Bulk RNA-Seq

For bulk RNA-Seq, Osx-Cre:GFP and Col1-GFP mice were dissected at E14.5 to isolate long bones, consisting of forelimbs and hind limbs, which were subjected to a digest using 2 mg/mL collagenase type II (Thermo Fisher Scientific) and 3 mg/mL dispase (Thermo Fisher Scientific) in serum-free αMEM for 30 min, in a shaking water bath at 37°C. This duration of the digestion was determined by an optimization procedure as explained in Figure S1A. Medium containing 10% FBS was added and the isolated cells were filtered (70μm), centrifuged at 100g for 10 min, washed with PBS, and resuspended at 1x 10^6 cells/mL in PBS containing 2% FBS. FACS based on GFP was done on a BD FACSAria Cell Sorter (BD Biosciences). Gates for Osx-Cre:GFP$^+$ and Col1-GFP$^+$ cell selection were set based on the FACS profile of GFP-negative control samples. Three samples per cell type were collected, each consisting of 300,000-550,000 cells originating from multiple embryos (see Figure 1B). Total RNA (850-1500ng per sample) was extracted using the RNeasy Micro kit (Qiagen), following the manufacturer's protocol. Library preparation using 400ng RNA was performed with the Illumina TruSeq Stranded mRNA Sample Preparation Kit (Illumina), according to the manufacturer's protocol. Denaturation of RNA was performed at 65°C and cooled down to 4°C. Samples were indexed to allow for multiplexing. Sequencing libraries were quantified using the Qubit fluorometer (Thermo Fisher Scientific). Library quality and size range was assessed using Bioanalyzer (Agilent Technologies) with the DNA 1000 kit (Agilent Technologies) according to the manufacturer's recommendations. Each library was diluted to a final concentration of 2nM and sequenced on Illumina HiSeq2500 generating 50 bp single-end reads with a sequencing depth of 30-40 Mb per sample. Splice-aware alignment was performed with TopHat v2.0.13 against the mouse mm10 genome. The number of allowed mismatches was 2. Reads that mapped to more than one site to the reference genome were discarded. The minimal score of alignment quality to be included in count analysis was 10. Resulting SAM and BAM alignment files were handled with Samtools v0.1.19.24. Quantification of reads per gene was performed with HT-Seq count v0.5.3p3 and Cuffquant (Cufflinks 2.2.1). Count-based differential expression analysis was done with R-based (The R Foundation for Statistical Computing, Vienna, Austria) Bioconductor package DESeq and Cufflinks 2.2.1. Reported p-values were adjusted (padj) for multiple testing with the Benjamini-Hochberg procedure, which controls for false discovery rate (FDR). For differential expression analysis of a single gene, DESeq datasets were used. To compare differential expression of multiple genes, cufflinks datasets were used, because this software includes a correction for gene length, rendering it possible to directly compare expression of multiple genes. Differentially expressed genes were identified based on the padj, with a padj<0.1 being considered statistically significant. Gene Set Enrichment analysis (GSEA) was performed with the GSEA software (MSigDBv6, Broad Institute) (Subramanian et al., 2005) using the gene lists with normalized reads.

Single cell (sc)RNA-Seq

For scRNA-Seq, 1 tibia and 1 humerus per embryo were isolated from 5 littermate Osx-Cre:GFP$^+$ embryos at E15.5 and pooled to one 'tibia' and one 'humerus' fetal limb cell sample, respectively. The collected tibia and humerus samples were next subjected to a digest of 2x 30 min using 2 mg/mL collagenase type II and 3 mg/mL dispase in serum-free αMEM at 37°C in a shaking water bath. Medium containing 10% FBS was added and the isolated cells were filtered (70μm), centrifuged at 100g for 10 min, washed with PBS, and resuspended at 2x 10^6 cells/mL in PBS containing 2% FBS. Right before cell sorting, 7'AAD viability Staining Solution (8 μl/ml) was added to the samples. FACS based on GFP was performed on a BD FACSAria Cell Sorter. Gates for Osx-Cre:GFP$^+$ cell selection were set based on the FACS profile of GFP-negative control samples. From each sample (tibia, humerus), 94 single cells were sorted into a 96-well plate containing lysis buffer (Milli Q water containing 0.2% Triton X and 2 U/ml RNase inhibitor). In addition, one 'no cell' and one 'multi-cell' control was collected per fetal limb sample. Plates were stored at -80°C until RNA extraction and scRNA-Seq was performed.

Amplification of the mRNA from single cells was performed using a modified Smart-seq2 protocol. One modification consisted of adding a 1 μl mix of biotinylated oligo-dT primer (5 μM; 5′-biotin-triethyleneglycol-AAGCAGTGGTATCAACGCAGAGTACT30VN-3′, where V is either A, C or G, and N is any base; IDT) supplemented with External RNA Controls Consortium spike-in mixture A (1:8,000,000 dilution; Thermo Fisher Scientific) to the cell lysate instead of the 1 μl of oligo-dT primer (10 μM) in the original protocol. During cDNA amplification 19 PCR cycles were used. The quality of the amplified cDNA was assessed using High Sensitivity DNA chips (Agilent) on the Bioanalyzer (Agilent). Sequencing was performed on a HiSeq4000 one lane in high output mode.

For scRNA-Seq data analysis, sequencing reads were trimmed with cutadapt 1.13 and aligned to the GRCm38 reference genome including ERCC sequences using STAR with default parameters (version 2.5.2b) as before (Wuidart et al., 2018). The gene expression count matrix was generated using HTSeq (version 0.6.0) on GENCODE M12 transcript annotations and counts for each protein coding gene were collapsed (Anders et al., 2015). The Scater R package (version 1.8.0) was used for quality control of the single cell samples: cells that complied with one of the following conditions were excluded: had fewer than 10^5 counts, showed expression of fewer than 3,000 unique genes, had more than 20% counts belonging to ERCC sequences, or had more than 25% counts belonging to mitochondrial sequences (McCarthy et al., 2017). After applying these cutoffs, 157 cells remained for downstream analysis. Genes for which fewer than 20 counts were observed across the complete dataset were excluded from further analysis. Read counts were, subsequently, normalized using the R package *scran* with default parameters (version 1.8.2). The R package SC3 (version 1.8.0) was used for the clustering, while PCA was performed employing the *prcomp* function in R based on the 2,000 most variable genes across the complete dataset (Kiselev et al., 2017). We chose k=3 for SC3 as this best represented the expected heterogeneity in our dataset. For cluster marker gene detection, we set the threshold to all genes with an AUC higher than 0.85 and

P<0.01. Heat maps and plots were generated using the pheatmap (version 1.0.10) and the ggplot2 (version 3.0.0) R packages, respectively. All data analysis was conducted in Python v3.6 (Python software foundation) or R v3.5.1 (CRAN).

Real-time quantitative RT-PCR (qRT-PCR)

To verify some of the RNA-Seq findings by qRT-PCR, we isolated fetal (E14.5) perichondrium-derived Osx-Cre:GFP$^+$ cells by enzymatic digest and FACS as described earlier in this paragraph for bulk RNA-Seq sample collection. As control cells, paired GFP-negative cell fractions were extracted from each perichondrial harvest taken from Osx:Cre-GFP(Tg) embryos. To isolate Osx-Cre:GFP$^+$ cells from newborn mice, the long bones of the forelimbs and hind limbs were dissected into samples consisting of a pool of bone shafts (excluding the cartilaginous epiphyses while maintaining the complete primary ossification center of the bones). The bone shafts were subjected to a full digest, using 3 mg/mL collagenase type II (Thermo Fisher Scientific) and 4 mg/mL dispase (Thermo Fisher Scientific) in serum-free αMEM (Thermo Fisher Scientific) for 2.5 h, in a shaking water bath at 37°C. Medium containing 10% FBS (GE Healthcare Life Sciences) was added and the isolated cells were filtered (70μm), centrifuged at 1000 rpm for 10 min, washed with PBS, and resuspended at 1–3 10^6 cells/mL in PBS with 2% FBS. FACS isolation of Osx-Cre:GFP$^+$ cells based on GFP-expression was performed on a BD FACSAria Cell Sorter. GFP-negative cell fractions were collected in parallel from each bone digest of the Osx-Cre:GFP(Tg) mice.

To compare gene expression in various primary cell populations, the following murine cell subsets were collected for RNA extraction: **(i)** newborn mCV OBs, **(ii)** mBMSCs, **(iii)** mOBs from 3-week-old mice, **(iv)** mOCLs differentiated from spleen. The cells were isolated and cultured as described below and harvested for RNA extraction (i) at passage 1 (n=3 samples, each derived from 3 calvaria) or (ii, iii) 5 days after initial seeding (n=4 samples, each derived from all femurs and tibias of one mouse) or (iv) at day 6 and 7 of mOCL differentiation. Direct isolation protocols were applied for: **(v)** newborn Osx-Cre:GFP$^+$ cells from long bones, isolated as described earlier in this paragraph (n=2 samples, each derived from bones of multiple mice). **(vi)** E14.5 ECs derived from the perichondrium of the long bones from forelimbs and hind limbs, released using 2 mg/mL collagenase type II (Thermo Fisher Scientific) and 3 mg/mL dispase (Thermo Fisher Scientific) in serum-free αMEM for 30 min, in a shaking water bath at 37°C. Medium containing 10% FBS (GE Healthcare Life Sciences) was added and the isolated cells were filtered (70 μm), centrifuged at 100 g for 10 min, washed with PBS, and resuspended at 10^6 cells/mL in PBS containing 2% FBS. Cells were stained with anti-CD45 (eBioscience) and anti-CD31 (eBioscience) antibodies for 30 min and washed with FACS buffer (PBS supplemented with 0.5% BSA), followed by FACS sorting of the CD45$^-$/CD31$^+$ cells (n=1 pooled sample containing mECs retrieved from 7 pups was collected for RNA extraction). **(vii)** Adult bone-derived ECs isolated from tibias and femurs of 10-week-old mice. Bones were dissected clean from surrounding tissues, flushed to discard the BM, cut into small fragments and washed with PBS. The fragments were digested using 3 mg/mL collagenase type II and 4 mg/mL dispase in serum-free αMEM for 2x 30 min in a shaking water bath at 37°C. Medium containing 10% FBS was added and the isolated cells were filtered (70 μm), centrifuged at 1000 rpm for 10 min, resuspended in FACS buffer (PBS supplemented with 0.5% BSA and 2mM EDTA) and counted. CD45-negative cells were isolated by reacting cells with CD45 MicroBeads (Milteny Biotec), loading them on a LD Column installed at a MidiMACS Separator (all from Milteny Biotec) according to the manufacturers protocol. Flow-through containing CD45$^-$ cells was next reacted with CD31 MicroBeads to retrieve CD45$^-$/CD31$^+$ cells. The yield from 4 mice was pooled to one RNA sample. **(viii)** Osteolineage cells and ECs from fracture calluses (Fx) were isolated from mice subjected to the semi-stabilized fracture model at 10 weeks of age. Calluses were harvested at PFD10, cleaned from surrounding muscle, chopped in pieces and digested and processed as above. The cells were resuspended in FACS buffer and reacted with PerCP/Cyanine5.5 anti-mouse CD45, PerCP/Cyanine5.5 anti-mouse TER119, a CD51 rat anti-mouse, PE and CD31 rat anti-mouse, PE-Cyanine7 antibodies for 30 min, followed by a wash with FACS buffer. FACS-sorted CD45$^-$/Ter119$^-$/CD51$^+$ cells (CD51$^+$ mOBs (Fx)) and CD45$^-$/Ter119$^-$/CD31$^+$ (mEC (Fx)) populations from 6 calluses were collected using a BD FACSAria Cell Sorter and pooled to one biological sample each.

To isolate RNA from cultured cells and cell lines (see further) we used the RNeasy Mini kit (Qiagen).

RNA from the fetal and newborn FACS-sorted cell samples was extracted using the RNeasy Micro kit (Qiagen). For RNA isolation of whole bones, isolated diaphyseal bone shafts, and callus tissue, the samples were crushed while frozen in liquid nitrogen and homogenized in Trizol (Sigma-Aldrich) as before (Dejaeger et al., 2017; Dirckx et al., 2018). RNA was separated from proteins, lipids and cellular debris using chloroform, and extracted with the RNeasy Mini kit.

Generally, cDNA was synthesized from 2 μg RNA, except from cells isolated by FACS or MACS where the RNA yield was lower, by incubation with 0.15 μg/μl Random Primers (Thermo Fisher Scientific) and 10 μl cDNA synthesis mix consisting of 2.5x buffer (Thermo Fisher Scientific), 25 mM dithiotreitol (DTT, Thermo Fisher Scientific), 1.25 mM dinucleotidetriphosphates (dNTP) (Thermo Fisher Scientific) and 50 U/μl Superscript reverse transcriptase (Thermo Fisher Scientific) according to the manufacturer's protocol. Gene expression was quantified using 2X TaqMan Fast Universal PCR Master Mix (Applied Biosystems) or the Fast SYBR Green Master Mix (Thermo Fisher Scientific) on a Step One Plus Real-Time PCR system according to the standard protocols. Primers are listed in the Table S3. Relative mRNA levels were calculated by the ΔΔCt method, using *Hprt* as housekeeping/reference gene, except for Figures 6J, 7A and 7K, where the housekeeping genes *18S* and *Rpl13a* were used when comparing gene expression across different cell lines.

Bone Analysis by Micro-CT, Histology and IHC

Micro-computed Tomography (micro-CT)

Micro-CT scans were made postmortem using a Skyscan 1172 device (Bruker) at 50 kV, 200 mA, and a 5 μm voxel size as described previously (Dejaeger et al., 2017; Dirckx et al., 2018). Scans were reconstructed and analyzed using Nrecon and CTAn software

(Bruker). For trabecular bone quantification in uninjured bones, a region of interest (ROI) containing 200 slices (1 mm) was selected starting at 250 μm below the growth plate. In this region, trabecular bone volume/tissue volume (BV/TV, %), trabecular number (Tb.N, mm^{-1}), trabecular thickness (Tb.Th, mm), and trabecular separation (Tb.S, mm) were determined. For cortical analysis, an ROI containing 100 slices (0.5 mm) was selected 2.5 mm below the growth plate to quantify the cortical thickness (Ct.Th, mm).

For analyses of fracture calluses, the ROI was determined as the callus region extending 200 slices (1 mm) in both the proximal and distal directions from the fracture site. The contours of the callus were manually drawn along the external boundaries of the callus, and at the periosteal surface of the original cortical bone. The resulting volume of interest (VOI), including the newly formed callus tissue but excluding the original cortex and medullary cavity, was taken as the callus tissue volume (Callus TV, mm^3). In this region, the callus bone volume (BV, mm^3) was determined to assess the amount of newly formed mineralized bone matrix; the relative bone mass was expressed as callus BV/TV (in %). The bone mineral density (BMD) was calculated from greyscale micro-CT images as the total bone mineral content (determined from hydroxyapatite (HA) phantoms of known density) within the VOI divided by the VOI volume (BMD, g HA/mm^3). 3D reconstructed models of the micro-CT bone scans were made using CtVol software (Bruker).

Histology and IHC of Frozen Tissue Sections

For histological analysis of embryonic bones, dissected samples were fixed for 4-6 h in 4% paraformaldehyde (PFA). Adult bone samples were fixed overnight in 2% PFA at 4°C and decalcified in 0.5 M EDTA for 2 weeks. Frozen samples were either embedded in Freeze Gel Q Path (VWR International) and cut into thin sections (5 μm), or embedded in 8% gelatin (Sigma-Aldrich) to generate thin (10 μm) and thick (40 μm) sections using a cryostat. In the former procedure, bones were first taken through a gradient of 30% D-(+)-Sucrose in increasing Freeze Gel Q Path medium and embedded by snap-freezing the samples in liquid nitrogen-cooled 2-methylbutane. For gelatin embedding, the tissues were cryoprotected using 20% D-(+)-Sucrose and 2% polyvinylpyrrolidone (PVP), according to a protocol generously shared by Prof. Marie-Helene Lafage-Proust (INSERM U 1059 Saint-Etienne and Université de Lyon, France).

For fluorescent immunohistochemistry (IHC) staining in thin (5 μm and 10 μm) frozen sections, unspecific antigen binding was blocked with TNB blocking reagent (supplied with the TSA Indirect Biotin System; PerkinElmer) before incubation with primary antibodies overnight at 4°C. The primary antibodies used in this study were rat monoclonal anti-CD31 (BD Pharmingen, 0.3 μg/ml), goat polyclonal anti-mouse CD31 (R&D Systems, 0.7 μg/ml), rat monoclonal anti-mouse endomucin (Emcn) (Santa Cruz, 4 μg/ml), chicken polyclonal anti-GFP (Abcam, 10 μg/ml), goat polyclonal anti-mouse PDGFRβ (R&D Systems, 2 μg/ml), rabbit monoclonal anti-VCAM1 (Cell Signaling Technology, 0.16 μg/ml), and a goat polyclonal anti-MMP-9 (R&D Systems, 2 μg/ml). To control for the specificity of the latter, a normal goat IgG control (R&D Systems, 2 μg/ml) was used and no specific binding was observed (data not shown). After primary antibody incubation, sections were washed in TNT and incubated for 1 h with appropriate secondary antibodies: Alexa Fluor 546-conjugated goat-anti-rabbit (Thermo Fisher Scientific, 20 μg/mL), Alexa Fluor 546-conjugated donkey-anti-rabbit (Thermo Fisher Scientific, 20 μg/mL), Alexa Fluor 546-conjugated donkey-anti-goat (Thermo Fisher Scientific, 20 μg/mL), goat-anti-rat IgG Fc DyLight 550 (Abcam, 5 μg/mL), donkey-anti-goat IgG H&DyLight 647 (Abcam, 20 μg/mL), Alexa Fluor 647-conjugated goat-anti-rabbit (Thermo Fisher Scientific, 20 μg/mL), or goat-anti-chicken IgY H&L DyLight 488 (Abcam, 5 μg/mL). CD31 (rat-raised) and Emcn signals were amplified using a polyclonal biotin-conjugated goat-anti-rat secondary antibody (BD Biosciences, 5 μg/ml) for 1 h followed by the TSA Cyanine 3 or 5 System (Perkin Elmer). Nuclei were visualized using Hoechst (Invitrogen, 5 mg/mL).

To visualize cell proliferation by BrdU incorporation, sections were subjected to treatment with proteinase K (1/1000) for 10 min and 4N HCl for 5 min before TNB blocking and incubation with rat monoclonal anti-BrdU (Novus, 3.3 μg/ml) overnight at 4°C. After primary antibody incubation, sections were washed with PBS and incubated for 1 h with goat-anti-rat DyLight 550 antibody (Abcam, 5 mg/mL). Nuclei were visualized using Hoechst (Invitrogen, 5 mg/mL). Cell proliferation by detection of EdU incorporation was visualized using the Click-iT™ EdU Alexa Fluor™647 Imaging Kit (Thermo Fisher Scientific) according to the manufacturer's instructions.

For IHC staining on thick (40 μm) gelatin sections, the tissue was permeabilized using 0.3% triton in PBS for 20 min at room temperature (RT) (except for PDGFRβ staining), followed by a blocking step using PBS supplemented with 5% serum, derived from the species in which the secondary antibodies were raised (donkey or goat normal serum), and 0.05% triton for 30 min at RT. Sections were incubated with primary antibodies in blocking solution overnight at 4°C. Primary antibodies included goat polyclonal anti-mouse CD31 (R&D Systems, 0.7 μg/ml), goat polyclonal anti-PDGFRβ (Santa Cruz Biotechnology, 2 μg/ml), and chicken polyclonal anti-GFP (Abcam, 10 μg/ml). Sections were washed thoroughly for 4 h with PBS and incubated with the appropriate secondary antibody for 75 min at RT. Secondary antibodies included goat anti-chicken IgY H&L DyLight 488 (Abcam, 5 μg/mL), donkey anti-goat IgG H&L Alexa Fluor 488 (Thermo Fisher, 20 μg/ml), donkey anti-goat IgG H&L DyLight 647 (Abcam, 20 μg/ml).

The stainings were imaged by wide-field fluorescence microscopy using an Olympus IX83 inverted microscope (Olympus) equipped with a DP73 camera or by confocal microscopy, either using laser scanning confocal microscopy on a Nikon C2 Eclipse Ni-E inverted microscope (Nikon) or through spinning disk confocal microscopy on a Nikon scope with Andor spinning-disk module microscope with dual camera (Ultra EMCCD 885).

Paraffin histology

The histological methods using paraffin sections of fetal, juvenile and adult mouse bones have been described in detail previously (Dejaeger et al., 2017; Dirckx et al., 2018). The bones were fixed overnight using freshly prepared 2% PFA at 4°C, decalcified in 0.5M EDTA for 2 weeks (only for postnatal samples), embedded in paraffin and sectioned at 5 μm. Paraffin sections were stained

with standard hematoxylin and eosin (H&E) or with a modified H&E protocol using Harris's acidified hematoxylin with mercuric oxide and eosin with phloxine B and orange G counterstain. Other sections were stained with Direct red 80 (Sirius Red) to visualize collagen fibers, with safranin O to visualize cartilage proteoglycans, or reacted for osteoclastic tartrate-resistant acid phosphatase (TRAP) activity using 0.5 mg/mL naphthol AS-MX phosphate (Sigma-Aldrich) and 1.1 mg/mL fast red violet LB (Sigma-Aldrich) followed by a fast green counterstain. E16.5 non-decalcified samples were stained according to Von Kossa's method for mineralized matrix. To visualize the vasculature, sections were subjected to IHC for CD31, as described above for frozen sections but using TSA Indirect Biotin System (PerkinElmer) with 3,3′-diaminobenzidine (DAB)-based visualization and brightfield detection, as before (Dirckx et al., 2018; Maes et al., 2006). Stained sections were imaged using an Olympus IX83 inverted microscope equipped with a DP73 camera.

MMA histology of undecalcified bones

For static and dynamic bone histomorphometry, tibias were isolated from uninjured mice, fixed in Burckhardt's solution overnight at 4°C, rinsed in 100% ethanol, and embedded in methyl methacrylate (MMA) without decalcification. 4 μm sections were stained with combined Von Kossa and Van Gieson stain, with toluidine blue, or left unstained to analyze the calcein labels, all as before (Dejaeger et al., 2017; Dirckx et al., 2018).

Histomorphometry

Measurements on histological sections were done using OsteoMeasure software (OsteoMetrics) or ImageJ software (NIH) on an Olympus IX83 inverted microscope equipped with DP73 camera. Analyses were in general performed blinded, on multiple sections per bone and the average values were calculated for each bone.

To assess bone developmental progression, stained paraffin sections of E16.5 tibias (1-4 sections per bone and per animal) were analyzed by histomorphometry, measuring the primary ossification center (POC) length (μm), the length of the chondro-osseous junction (corresponding to the width of the fetal bone at the level of the last row of hypertrophic chondrocytes of the growth plate), and the blood vessel density at the chondro-osseous border (number of blood vessels per unit of length).

H&E-stained paraffin sections of P10 tibias and femurs were used to quantify the size of the forming secondary ossification center (SOC) (4 sections per bone). Quantification of the blood vessel (BV) density at the chondro-osseous junction of growing tibias at P10 was performed on CD31-stained sections (1 section per bone).

Histomorphometric analysis of the fracture callus of control and PDGFRβ cKO mice included the following measurements, performed using Image J and OsteoMeasure software, by manual lining and marking of the specified structures on the stained sections: (i) amount of cartilage represented by the Safranin O (red)-stained area, expressed in absolute values (mm^2) and as fraction (% of callus area); (ii) fibrotic tissue (absolute and as fraction of the callus area) as detected on H&E/orange G-stained sections; (iii) the number of $CD31^+$ blood vessels (BV) in the callus, the average BV size, and BV area as measure of callus vascularization, either in absolute terms or quantified as fraction of the callus area taken up by vessels and their lumens on CD31-stained paraffin sections; and (iv) the number of adipocytes, and the area occupied by adipocytes in the proximal metaphysis and bone marrow of fractured tibia, as counted and measured on H&E-stained sections. Each analysis was performed on a minimum of 3 sections per mouse, except for the adipocyte quantification which was performed on 1-2 sections per mouse, and the average values were calculated for each bone.

Cryosections stained for BrdU (red) and depicting Osx-Cre:GFP+ cells (green) were used to quantify the periosteal response to bone trauma at PFD3. Briefly, regions of periosteal expansion, taken from the fracture site to maximally 500 μm distant therefrom, were manually lined using ImageJ and averaged to obtain the periosteal area. The maximum periosteal thickness was measured. Within the periosteal area, Osx-Cre:GFP^+ cells were detected using Image J and automatically counted; only signals present in both the green (GFP) and blue (Hoechst) channels were selected to minimize artificial fusion of neighboring cells during GFP^+ quantification. The $BrdU^+$ (red)-stained Osx-Cre:GFP+ cells were counted manually and the % of $BrdU^+/Osx^+$ cells was calculated. Analyses were performed on 2-3 sections per bone and the average values were calculated for each bone.

For nearest neighbor distance analyses quantifying the distances between Osx-Cre:GFP^+ cells (green) and the nearest $CD31^+$ blood vessel (red fluorescent IHC staining on cryosections), the thresholded green and red channels were analyzed using the interaction analysis component of the Image J plugin Mosaic with radius, cutoff and per/abs settings of 3:1:1 and 1:1:1 for the green and red channels, respectively. Analyses were performed 3 sections per bone.

Standardized static and dynamic bone histomorphometry to determine the osteoblast and osteoclast-related parameters relevant for bone remodeling, was performed in the proximal tibia, measuring on average 3 sections per bone using OsteoMeasure software (OsteoMetrics) as detailed before (Dejaeger et al., 2017; Dirckx et al., 2018) and indicated in Table S1.

Cell Cultures and *In Vitro* Assays

Primary cell isolation, culture, transduction

For mBMSC cultures, femurs and tibias were isolated from 3-week-old or 6-8-week-old mice and thoroughly cleaned to remove muscles and connective tissues. Epiphyses were removed with a sterile scalpel and each bone shaft was placed in a Heparin coated Microvette CB tube (Sarstedt) to centrifuge for 2 min at 4500 rpm. The BM plug in the collection tube was resuspended and plated in DMEM containing 15% FBS and 1% AA (only for growth curve experiment, Figure 5A) or in DMEM containing 20% non-heat-inactivated FBS and 1% AA (all other experiments with mBMSCs).

Primary mCV OBs were derived from newborn wild type CD1 mice, *PDGFRβ*$^{(lox/lox)}$ mice or PDGFRβ cKO and control mice by enzymatic digestion. Three calvarias were pooled per sample and digested using 2 mg/mL collagenase type II and 3 mg/mL dispase in

serum-free αMEM, shaking at 37°C, during six 10-min time intervals. The first digest, with moderate shaking (250 rpm), was discarded. Digestions two to six, with rigorous shaking (400 rpm), were collected in αMEM with 10% FBS. The harvests were filtered, centrifuged, resuspended, and cultured in αMEM containing 10% FBS and 1% AA. After overnight incubation, the medium was refreshed to discard non-adherent cells, and the cells were further grown to confluence. At passage 1, *PDGFRβ*$^{(lox/lox)}$ calvaria cells were transduced with adenoviruses (multiplicity of infection [MOI] 800) containing either an Ad5CMVempty vector (AdEmpty, Viral Vector Core) or a Ad5CMVcre vector (AdCre, Viral Vector Core) to recombine and inactivate the *PDGFRβ* gene *in vitro*, as described previously (Dejaeger et al., 2017; Dirckx et al., 2018). Cells were subsequently seeded at a density of 40,000 cells/cm^2 in 12-well plates. All analyses were performed 96 h post-transduction.

Long bone mOBs from 3-week-old mice were isolated from tibias and femurs that were dissected clean from surrounding tissues, flushed to discard the marrow, cut into small fragments and washed with PBS. The fragments were digested using 3mg/ml collagenase and 4mg/ml dispase at 37°C. The first digest (15 min, shaking at 250 rpm) was discarded, and the subsequent 3 digests (30 min each, at 400 rpm) were collected in αMEM + 10% FBS + 1 % AA, filtered, centrifuged, and cultured.

For mPDC cultures, femurs and tibias from 6-8-week-old mice were isolated and cleaned from muscles and connective tissue without damaging the periosteum. As described by (van Gastel et al., 2014) the epiphyses were next submerged in 5% Ultra Pure LMP Agarose (low melting point) (Thermo Fisher Scientific) until solidified. Subsequently, the bones with their epiphysis covered in agarose were incubated in digest medium consisting of 3 mg/ml collagenase type II and 4 mg/ml dispase in αMEM, at 37°C. The first 10-min digest at 250 rpm, primarily removing remnant soft tissues, was discarded. The yield from the next digest (60 min at 400 rpm, releasing the mPDCs) was cultured in αMEM containing 10% FBS and 1% AA. The yield from 3 mice (2 tibias and 2 femurs each) was pooled and filtered, centrifuged, resuspended, and cultured in T25 flasks.

For mOCL differentiation, spleen cells were isolated from 10- to 12-week-old mice by dissociating the spleen over a 70 μm cell strainer. Spleen cells were collected in αMEM + 10% FBS + 1 % AA, centrifuged, and plated at a concentration of 200,000 cells/well in a 24-well-plate. Osteoclast differentiation was induced by adding rmRANKL (R&D Systems, 100 ng/ml) and rmM-CSF (R&D Systems, 20 ng/ml) to the culture medium. Differentiation medium was refreshed at day 4 and cells were harvested at days 6 and 7.

Cell line transfection

An MC3T3-E1 cell line overexpressing VCAM-1 (*VCAM-1 OE*) was generated by transfecting MC3T3-E1 cells seeded in a 6-well plate at 60-80% confluency with 1 μg/ml of a Vcam-1 mouse cDNA clone (OriGene) using 30 μl/ml lipofectamine 2000 (Thermo Fisher Scientific) diluted in OPTIMEM (Thermo Fisher Scientific). Cells transfected in parallel with 1 μg/ml pCMV-Entry Tagged Cloning Vector plasmid (OriGene) were used as control cells. To select for cells containing the plasmid, cells were subjected to treatment with 0.5 mg/ml neomycin (G-418 Solution, Roche) for 7 days. Surviving cells were cultured with low selection pressure using standard MC3T3 medium as described above supplemented with 0.2 mg/ml neomycin. The overexpression of VCAM-1 was verified by qRT-PCR.

Inhibitor and recombinant protein treatment

In experiments assessing *MMP-9* expression regulation, cells were seeded into standard well plates and, at 60-80 % confluency, treated with molecular inhibitors against PDGFRβ (Imatinib, Selleckchem, 5μM), PI3K (Wortmannin, Selleckchem, 100nM), AKT (Perifosin, Selleckchem, 10 μM), RAF/MEK (RO5126766, Selleckchem, 1 μM) and ERK1/2 (SCH772984, Selleckchem, 2 μM). After 3 h pre-treatment, rhPDGF-BB (R&D Systems, 5ng/ml) or vehicle was added to the cells for 5 h. RNA was extracted and *MMP-9* transcript levels relative to *HPRT* were quantified by qRT-PCR. To asses MMP expression after treatment with various growth factors, cells were incubated for 16 h with rhPDGF-BB (R&D Systems, 5ng/ml), rhPDGF-DD (R&D Systems, 5ng/ml) or rhVEGF165 (R&D Systems, 5ng/ml) prior to RNA extraction.

Cell growth and proliferation assays

Cells were seeded in a 12-well plate at 20-40% confluency and treated over a period of up to 7 days with rhPDGF-BB (5 ng/ml), Imatinib (5 μM), or a combination of both, with the medium being changed daily (for cell lines) or every other day (primary cells). To establish the growth curve, cell numbers were quantified by cell counting (cell lines) or DNA quantification (primary cells) at the indicated time points during the treatment (from day 0 until day 6). To determine the DNA content (indirectly reflecting cell number; used as measure of cell growth and as normalization parameter in osteogenic differentiation assays (see further)) cells were incubated in DNA extraction homogenization buffer for 1 h at 37°C and homogenized using cell scrapers. After addition of Hoechst (2 mg/ml) the DNA content was measured at a fluorescence of 360nm/460nm excitation and emission, respectively, and calculated based on a herring sperm DNA-based standard curve.

To evaluate ST2 cell proliferation by BrdU incorporation, cells receiving the same treatment were incubated at day 3 for 6 h with BrdU (Roche, 10 μM). Afterwards, cells were fixed with 4% PFA and BrdU was visualized by antibody staining. Briefly, cells were treated for 10 min with proteinase K (Sigma-Aldrich, 2U/g) followed by an incubation of 5 min with 4N HCl. After blocking with TNB for 30 min, cells were incubated with rat monoclonal anti-BrdU (10 μg/ml) overnight. After a washing step, goat anti-rat IgG Fc DyLight 550 secondary antibody (0.5 mg/ml) was added for 1 h and nuclei were visualized using Hoechst (5 mg/mL).

To evaluate mBMSC proliferation by EdU incorporation, cells were pretreated with rhPDGF-BB (5 ng/ml), Imatinib (5 μM) or a combination of both components for 16 h before EdU was added for 5 h. Afterwards, cells were fixed with PFA and incorporated EdU was visualized using the Click-iT EdU Imaging Kit. Per independent biological experiment, in total 12 images for each condition were analyzed blinded, by quantifying the number of EdU$^+$ over Hoechst$^+$ nuclei.

Cell migration and invasion assays

Scratches were made in confluent MC3T3 cell layers as before (Dejaeger et al., 2017). Cells were treated with rhPDGF-BB (R&D Systems, 5 ng/ml), Imatinib (5 μM), Orantinib (5 μM) or Amuvatinib (5 μM) (all from Seleckchem) in αMEM with 1% FBS, with equal volumes of vehicle added to control wells. Conditioned medium (CM) was prepared by culturing a HUVEC or MC3T3-seeded 60-80% confluent T75 flask (Greiner) with 8 ml of media for 24 h; the medium was collected, sterile filtered using a 0.22 μm filter (Millipore) and stored at -80°C until use. In experiments co-culturing HUVECs and MC3T3 cells, the total number of MC3T3 cells was maintained constant and only MC3T3 cells migrated in the timeframe of the study (confirmed by membranous labeling of the respective cell types with green and red dyes (not shown)). Scratch closure (%) was calculated as the change in the cell-free area of the culture recipient between time 0 and 14 h. Cells were stained with Hoechst (5 mg/ml) and Alexa Fluor 488 phalloidin (Thermo Fisher Scientific).

To investigate migration of mCV OBs, cells were seeded into an ibidi chamber (ibidi GmbH). At confluency, the chamber was removed and cells were treated with vehicle, rhPDGF-BB (R&D Systems, 5 ng/ml), Imatinib (5 μM), or rhPDGF-BB and Imatinib combined. To prevent cell proliferation, 1 μg/ml mitomycin was added to all conditions. Cell movement into the cell-free area was monitored by live imaging over 24 h, capturing and quantifying images every 15 mins.

For determining cell invasiveness through matrix components, 25,000 cells treated with or without MMP-9 inhibitor I (Merck Millipore, 100 nM) or the pro-MMP-9 activation inhibitor JNJ 0966 (R&D Systems), were seeded in a 6.5 mm Corning Transwell polycarbonate membrane cell culture insert (Sigma-Aldrich Aldrich, 8 μm pore size membrane) which was coated with rat tail-derived collagen type I (Corning, 0.5 mg/ml), growth factor-reduced Matrigel (Corning, 1 mg/ml) or gelatin solution (Sigma-Aldrich, 2%) and placed on a well containing rhPDGF-BB (10 ng/ml) in DMEM supplemented with 1% FBS. After 15 h, cells were fixed with 4% PFA and nuclei were stained with Hoechst (2 mg/ml). Fluorescent images were taken and cell invasiveness was determined by counting the nuclei at the down-side of the insert membrane. Per independent biological experiment, in total 8-10 images for each condition were analyzed blinded.

Osteogenic differentiation assay

Cells were cultured for up to 7 days (mBMSCs) or 21 days (mCV OBs, ST2 cells) in osteogenic differentiation medium (DMEM containing 20% FBS for mBMSCs and 10% FBS for other cells, 1% AA, 250 μM L-ascorbic acid and 10 mM β-glycerophosphate (Sigma-Aldrich)) supplemented with rhPDGF-BB (R&D Systems, 5 ng/ml), Imatinib (5 μM) or a combination of rhPDGF-BB and Imatinib. Medium was refreshed three times per week. At day 0 and indicated time points during the differentiation protocol, cells were fixed with ice-cold methanol for 30 min and stained with 1% Alizarin red S solution (pH4.2, Sigma-Aldrich) for 2 h at RT to analyze mineralized matrix production. After washing and imaging the wells, the dye was extracted using 10% acetic acid to quantify the staining. Absorbance was measured at 405nm and normalized for DNA content (DNA extraction as above). RNA of mCV OBs was harvested for gene expression analyses at day 0 and 21.

Osteo-angiogenic affinity assay

To analyze osteogenic cell recruitment to endothelial tubules, 300 μl of growth factor-reduced Matrigel (Corning) was added to 24-well plates, allowed to solidify at 37 °C for 30 min, and then seeded with 75,000 HUVECs or MS1 cells stained with 5 μl/ml Vybrant DiI (red) membrane labelling dye (Thermo Fisher Scientific). After 4 h, endothelial tubules had formed on the Matrigel, and MC3T3-E1 cells labeled with 5 μl/ml Vybrant DiO (green) membrane dye (Thermo Fisher Scientific) were added to the network. When indicated, cells were pre-treated with Imatinib (5 μM) for 30 min before adding them to the tubules. The experiment was conducted in a 1:1 mix of the specific culture media for the respective cell types, supplemented with 1% FBS. Fluorescent and bright-field images were taken 2 h after MC3T3 addition. Per independent biological experiment, in total 10 images for each condition were analyzed blinded. The total tubule length of the endothelial lattices was measured (finding no differences in the vascular network between the conditions, data not shown) and the number of osteogenic cells (total number per field of view as well as the number of cells found in association with tubules, calculating the % of cells on tubes) was quantified using Image J.

Cell-cell adhesion assay

To test adhesion between OBs and ECs, MS1 cells were first grown to a confluent cell layer. Control or *VCAM-1 OE* MC3T3-E1 cells were labeled with Vybrant DiO (Thermo Fisher Scientific) and seeded on top of the MS1 feeder layer. After 3 h, non-adherent cells were removed by rinsing with PBS, and fluorescent and brightfield images were taken. Per independent biological experiment, 5 images for each condition were analyzed blinded. The number of adherent cells was determined by counting the DiO^+ cells per field of view.

QUANTIFICATION AND STATISTICAL ANALYSIS

Analysis of RNA-Seq data is detailed in the respective sections above. Briefly, padj<0.1 by the Benjamini-Hochberg procedure was used as threshold for statistical significance. All other statistical analyses were conducted using GraphPad Prism. Two sample groups were generally compared by unpaired, two-sided Student's t-tests (unless specified differently, as in Figure 5E where paired testing was performed between treatments of individual cell pools) or, in case of unequal variances, using unpaired, two-sided Student's t-tests with Welch's correction. Data of more than two groups were analyzed by 1way ANOVA followed by Tukey's post-hoc test or 2way ANOVA followed by Sidak's post-hoc test, unless specified differently in the legend (as for Figures 5A and 5G). In the case of unequal variances, Kruskal-Wallis test was performed. The specific test used is indicated in the respective figure legend.

Values of $p<0.05$ were considered significant and are indicated as: *$p<0.05$, **$p<0.01$, ***$p<0.001$. *n* numbers are biological repeats, representing (i) the number of individual mice per genotype group for *in vivo* data, (ii) independent cell pools derived from separate (sets of) animals for primary cell cultures, or (iii) independent experiments when using cell lines. Measurements are represented in the graphs or tables as mean ± SEM.

DATA AND CODE AVAILABILITY

The RNA-Seq datasets generated in this study are available at the European Nucleotide Archive (ENA). The project accession number for the bulk RNA-Seq data is ENA: PRJEB33441. The project accession number for the scRNA-Seq files reported in this paper is ENA: PRJEB33444.